ION-INDUCED CHARGE EMISSION FROM SURFACES BOMBARDED BY AN [EMIM][BF_4] ELECTROSPRAY PLUME

BY

MATTHEW RICHARD KLOSTERMAN

THESIS

Submitted in partial fulfillment of the requirements
for the degree of Master of Science in Aerospace Engineering
in the Graduate College of the
University of Illinois Urbana-Champaign, 2021

Urbana, Illinois

Adviser:

Associate Professor Joshua L. Rovey

ABSTRACT

Experiments have been conducted at the University of Illinois at Urbana Champaign Electric Propulsion Laboratory to study the ion-induced secondary charge emission from surfaces bombarded by an [Emim][BF_4] electrospray plume. The effect of changing the bias from -85 to +85 V on a target collecting current from the electrospray plume has been measured. These data are used to calculate the yield of positive and negative charged species emission from the target due to bombarding cations and anions. The yields of positive charges per incident cation (γ^+_{cation}), negative charges per incident cation (γ^-_{cation}), positive charges per incident anion (γ^+_{anion}), and negative charges per incident anion (γ^-_{anion}) are measured for eight different industrial materials commonly used in electrospray diagnostics or thruster and spacecraft construction. These yields range from 0-1.3 charges per incident ion over a range of emitter voltages from 1.5-2.9 kV and largely display linearly increasing trends with increasing emitter voltage. Over this emitter voltage range, γ^+_{cation} ranges from 0-0.55, γ^-_{cation} ranges from 0-0.75, γ^+_{anion} ranges from 0-0.4, and γ^-_{anion} ranges from 0.3-1.3. The data show for the first time positive and negative charges being emitted due to both cation and anion bombardment, and suggests that secondary ions sputtered from the target material, oxide and hydrocarbon surface layers, and an accumulated ionic liquid layer are important to the secondary charge emission behavior of electrospray plumes.

ACKNOWLEDGEMENTS

Firstly, thank you to my adviser, Dr. Rovey, for his support and sharing his knowledge and expertise. This project would not have succeeded without your guidance and feedback. Thank you to Dr. Levin and her students Neil, Victor, Nakul, and Siddharth for their collaboration and repeated explanations of what exactly it is that they're doing. Thanks also to Tom Liu at NASA Glenn Research Center for overseeing this project.

Thank you to all members of the EP Lab who I had the pleasure of working alongside. Specific thanks to Alex for giving me the guidance and mentorship that brought me here. Your friendship has meant a lot to me. Thanks to Chris for sharing ideas and confusion about electrosprays (and for being a great tennis partner), thanks to Matt and Matt, Hussein, Toyo, Emil, and Nick for your friendship and for making up the Friday lunch crew. Thanks also to Avinash for continuing the work I've started here.

Thanks to Rick Haasch and Tim Spila at the Materials Research Lab for their help with surface measurements. Thanks to the AE machine shop crew for always being available and for catching my mistakes on machine drawings. Thanks to Dr. Ben Prince and Dr. Shawn Miller at AFRL for showing me the ropes when it comes to electrospray. A huge thank you to Kapton tape for literally holding my project together.

Thank you to my family and friends from St. Louis and Rolla who have supported me from a distance and helped me find my way here. Lastly, a great thanks is due to my wonderful and beautiful fiancée, Brittney. Seeing you at the end of long weeks in the lab helped me keep it together many times and your support helped me when I felt lost. I couldn't have done any of this without you.

TABLE OF CONTENTS

LIST OF FIGURES

LIST OF TABLES

NOMENCLATURE

γ_{cation}^{+}	=	yield of positive charges per impinging cation
γ_{cation}^{-}	=	yield of negative charges per impinging cation
γ_{anion}^{+}	=	yield of positive charges per impinging anion
γ_{anion}^{-}	=	yield of negative charges per impinging anion
γ_{Adj}	=	adjusted electron emission yield
γ_{Theo}	=	theoretical electron emission yield
$I_{emitter,c}$	=	emitter current measured in cation electrospray mode, nA
I_{cation}^{+}	=	positive secondary current from target bombarded by cations, nA
I_{cation}^{-}	=	negative secondary current from target bombarded by cations, nA
$I_{emitter,a}$	=	emitter current measured in anion electrospray mode, nA
I_{anion}^{+}	=	positive secondary current from target bombarded by anions, nA
I_{anion}^{-}	=	negative secondary current from target bombarded by anions, nA
$I_{Secondary}$	=	secondary current emitted from the target surface, nA
$I_{Emitter}$	=	current measured at the externally wetted emitter, nA
$I_{Extractor}$	=	current measured at the extractor, nA
I_{Target}	=	current measured to the target, nA
I_{Norm}	=	normalized current collected during RPA
I_{Plume}	=	current of the electrospray plume downstream of extractor, nA
$I_{Impinging}$	=	current from the emitter impinging upon the extractor, nA
I_{Return}	=	secondary current which travels upstream to the extractor, nA
KE	=	kinetic energy, keV
m_{dimer}	=	mass of a dimer ion, amu

$m_{monomer}$	=	mass of a monomer ion, amu
RMS	=	surface roughness, µm
SPK	=	mean peak height, µm
SVK	=	mean valley depth, µm
$V_{Emitter}$	=	emitter voltage, kV

CHAPTER 1

INTRODUCTION

Electrospray propulsion has quickly become a promising candidate for small satellite propulsion. In electrospray thrusters, ions and/or droplets from room-temperature ionic liquids (IL) are electrostatically extracted and accelerated to high velocities (>10,000 m/s) to provide thrust. Recent development has focused on porous-glass electrospray thrusters [1–3], which passively feed the IL through a porous glass substrate with machined tips towards a charged extraction grid. These thrusters typically emit in a pure-ion regime in which the plume mainly consists of single ions (monomers) or ions attached to a neutral pair (dimers), resulting in very high specific impulse (>1500 s).

An important aspect of any electric propulsion (EP) systems is accurate modelling and understanding of the plume ion-surface interactions. High energy ions impinging on a surface cause sputtering (removal of surface atoms) and ion-induced electron emission (IIEE). Many spacecraft designers were initially hesitant to use ion or Hall thrusters for their missions, and the EP community dedicated decades to experimental and modeling research to understand these surface interactions for xenon plasma ions. The data from these experiments is used in plume-surface interaction models to estimate thruster lifetime and model spacecraft contamination and charging. Results are used by spacecraft designers and the effects of xenon EP systems are now understood well enough to be used on low-risk commercial and government missions. While xenon-based EP plume ion-surface interactions are relatively well understood, at least to the point where models are being used to integrate EP onto spacecraft, the study of ion-surface interactions for electrospray plumes is very much in its infancy.

Early research on electrospray plume ion-surface interactions has focused on sputtering yields from electrospray plumes impinging on surfaces and has found that yields up to 6 atoms per impinging molecule are possible and that chemical reactions between the ion and surface may be an important sputtering mechanism [4,5]. However, each of these studies focused on capillary electrospray emitters that emit primarily charged droplets consisting of 100s-1000s of molecules and not the pure-ion monomer and dimer plumes of porous glass electrospray thrusters. No experimental work has been performed to study sputtering of electrospray plumes in the pure-ion regime and attempts at molecular dynamics models of electrospray plume sputtering have largely not agreed with the existing experimental data for droplet-surface sputtering [6].

Recent literature identifies anomalous thruster test results that may be due to plume-surface interactions. Testing of electrically isolated thruster systems, similar to a spacecraft configuration, has shown anomalous spacecraft charge loss [7] when the thruster is operated in anion mode and then turned off. Possible explanations of this charge loss is plume ions returning to the charged spacecraft and causing IIEE, or plume ions impinging on facility surfaces and generating secondary positive charges that return to the spacecraft. The University of Southampton reported possible IIEE interference in time-of-flight measurements when negative currents were measured during cation mode experiments and in anion mode the currents did not return to zero after the plume was impeded [2]. Experiments at Massachusetts Institute of Technology suggest IIEE from a faraday cup explains anomalous retarding potential analyzer (RPA) traces of anion energy distribution [8]. The University of Southampton has performed an electron emission suppression study using a negatively biased nickel grid to suppress electron emission from an aluminum plate that collects current from a porous glass electrospray thruster plume [9]. The method of using a negatively biased grid to suppress electron emission is common in electrospray diagnostics, but,

as discussed in later sections, may not provide a full picture of the ion-surface charge emission mechanism and the experimental results obtained may be more complicated than commonly assumed. Recent modelling work at UCLA has calculated a theoretical electron emission yield vs. ion energy relationship for a stainless steel surface bombarded by an electrospray plume [10]. As discussed in later sections, a wider range of data is needed from both modelling and experimental groups to make useful comparisons and more advanced models are needed to capture all aspects of the complicated experimental systems. To understand and adequately account for plume-facility interactions in future experimental electrospray research more information is needed about the charge emission behavior of surfaces bombarded by electrospray plumes.

The following sections describe experiments that investigate the charged species emitted from common thruster, facility, and spacecraft materials bombarded by an electrospray plume operating in pure ion regime. Charge collecting surfaces are often biased positive, or a grid is biased negative, to suppress electron emission from the collector, and the experiments described here provide information on the charge emission mechanisms taking place in these systems and prompt questions regarding unknown effects that have yet to be investigated. Results here for the first time show the effect of emitter voltage, operating polarity, and surface material on the yield of charged species, including evidence of emitted secondary ions along with emitted electrons. The experimental setup is described in the next section followed by the experimental results, analysis, and conclusions.

CHAPTER 2

EXPERIMENTAL SETUP

Facility Description

The electrospray experiments are performed in a 24” dia. x 27” vacuum chamber equipped with one CTI Cryo-Torr 8 cryopump powered by a Brooks 9600 helium compressor and roughed by a dry mechanical pump. The chamber has a base pressure of $2x10^{-6}$ Torr and all experiments are performed at an operating pressure below $3x10^{-5}$ Torr. Inside the chamber, a Newmark Systems RM-3 rotary stage is mounted on an optical breadboard plate with a mount for an electrospray emitter/extractor assembly.

Emitter Properties

A single etched 0.5-mm-diameter tungsten wire externally wetted emitter is used as the electrospray source in all experiments. This type of emitter is well characterized in the literature [11,12] and typically emits in the pure-ion regime similar to a porous glass electrospray thruster [2]. The emitter is electrochemically etched following the procedure in [11] and further details are given here. The tip is dipped in a 1N NaOH solution at 50 V until there is a smooth, concave curvature from the wire to a rounded point. A 0.25 mm diameter tungsten wire is spot welded orthogonally ~3 mm from the tip to provide an IL reservoir. The tip/reservoir assembly is submerged for 45 seconds in a 2N NaOH solution saturated with $K_3Fe(CN)_6$ at 90-95°C to roughen the surface of the emitter for better fluid transport to the tip. The resulting emitter has a tip radius

of curvature of ~32 mm and is shown in Figure 1a. The emitter with the crossbar attached and mounted in its copper holder is shown in Figure 1b.

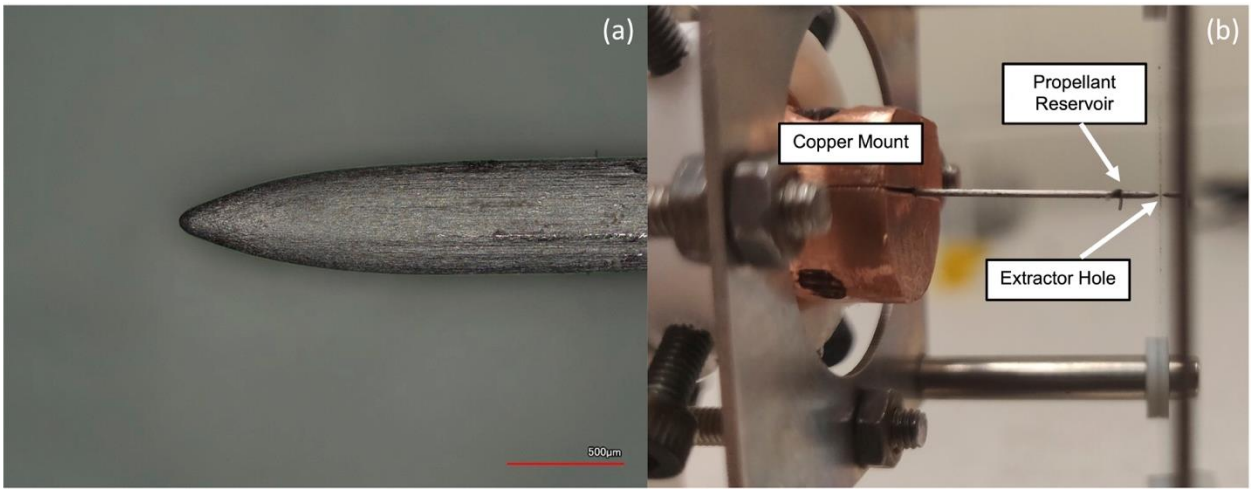

Figure 1: Tungsten wire externally wetted electrospray emitter (a) up close and (b) mounted in front of the 1.4 mm hole in the extractor grid

Before testing, the emitter is ultrasonically cleaned in distilled water for 10 minutes, then in ethanol for 10 minutes to remove the water. After drying with compressed air, a heat gun is used to heat the tip/reservoir assembly for 1 minute to increase wettability of the surface. A syringe is then used to drag a drop of [Emim][BF_4] over the tip and back to the reservoir while ensuring that the emitter is wetted on all sides. The emitter is mounted on a copper block that serves as an electrical lead and heat sink. A 1 mm thick stainless steel extractor plate has a 1.4 mm diameter hole centered on the emitter tip and is located 0.1 mm downstream of the emitter tip. The entire assembly is mounted in the vacuum facility as described above and the chamber is pumped down to operating pressure.

Electrical and Diagnostics Setup

A photograph and schematic of the experiment setup are shown in Figure 2. The emitter and target are each connected to a Matsusada AMS-5B6 high voltage amplifier. The extractor is

grounded for all experiments here. The emitter is operated in a 1 Hz square-wave AC mode with a peak-to-peak value of 2x the emitter bias voltage. A custom high-voltage current monitor is connected between each amplifier and the emitter and target. This current monitor consists of a TI AMC1311 isolation amplifier that amplifies the voltage drop across a 1 MΩ shunt resistor on the high voltage side and outputs a differential signal at ground with a gain of one. Because the isolation amplifier is a single-polarity device, a diode is used to direct the current towards different amplifiers for positive and negative emission mode measurements. Each of these custom current monitors was tested by being placed in series with a 1 GΩ resistor followed by a Keithley 6514 electrometer. A 0.5, 1, 1.5, and 2 kV magnitude square wave was then applied across the circuit and the currents measured by the electrometer were compared to the currents measured by each of the custom current monitors and the maximum difference was ±9.62%. This error is illustrated in the error bars of all current measurements as well as quantities calculated from current measurements. The current to the extractor is measured using a Keithley 6514 electrometer.

A Kimball Physics FC-71A faraday cup with retarding potential analyzer (RPA) grids is mounted to one side of the emitter. Current to the faraday cup is measured by a Keithley 6514 electrometer and the retarding grid is biased using a Matsusada AMS-5B6 high voltage amplifier. The faraday cup is used to measure the plume current density distribution and plume ion energy distribution, and results are compared with literature data for other emitters to verify similar or typical operation. A National Instruments (NI) USB-6211 data acquisition unit measures analog signals from all instruments and controls the high-voltage amplifiers via analog output. Data are recorded on a PC using the NI DAQExpress software.

For plume-surface interactions experiments, the emitter is aimed at a 15x15 cm target of the material of interest. The target is mounted 8 cm from the extractor as illustrated in Figure 2a

resulting in a 43° capture angle of the plume – far greater than the measured 17° divergence half-angle – such that the entire plume impinges on the target. For the experiments using tungsten carbide, molybdenum, and gold targets, the size of the target was limited by material cost and so the target was placed 1 cm from the extractor to capture the entire electrospray plume. The emitter is operated in AC mode at 1 Hz and the currents to the emitter and extractor are measured as described above. Current is measured at the target, emitter, and extractor as the DC bias voltage on the target plate is adjusted from -85 to +85 V.

It is important to the interpretation of the data in these experiments to understand the possible sources (and sinks) of charge and the corresponding effect on the measured currents, as illustrated in Figure 2b. The high voltage of the alternating bipolar supply creates a strong electric field between the emitter and extractor, and positive or negative (cation or anion) charge is emitted from the emitter ($I_{Emitter}$). A small fraction of the emitter current impinges on the extractor grid ($I_{Impinging}$) and is always < 5% such that $I_{Plume} \approx I_{Emitter}$ for the experiments described here. The impinging current is measured in the extractor current ($I_{Extractor}$) as described in Equation 1. The emitter current that passes through the extractor orifice is the plume current (I_{Plume}) as described by Equation 2. All of the plume current is incident on the target and may give rise to secondary charge emission from the target. The measured target current (I_{Target}) is the result of the plume current and any secondary emitted current ($I_{Secondary}$) as described in Equation 3. In the absence of secondary current, all the plume current is collected at the target ($I_{Plume} = I_{Target}$). In most experiments though, this is rarely the case because of secondary emission current from the target. For example, electrons, or other negative charges, leaving the target surface result in a more positive current being measured at the target (because $I_{Secondary} < 0$), whereas positive charges leaving the surface result in a more negative current being measured at the target (because

$I_{Secondary} > 0$). For example, electron emission caused by incident plume cations results in a larger positive current being measured at the target than the total plume cation current ($I_{Target} > I_{Plume}$).

Still referring to Figure 2b, we find that secondary charge emitted from the target can travel upstream and be collected by the extractor. We define this as the return current (I_{Return}) such that the total measured extractor current is the sum of the impinging current from the emitter and the return current from the target as described by Equation 1. In some cases (when the target is close to the extractor), nearly all the secondary current is collected at the extractor ($I_{Secondary} \approx I_{Return}$), but in other cases (when the target is farther away) much less secondary current is collected at the extractor ($I_{Return} \neq I_{Secondary}$). In this latter case, we assume that the secondary current is finding its way to ground through the facility walls or other grounded components of the setup whose current is not measured.

$$I_{Extractor} = I_{Impinging} + I_{Return} \tag{1}$$

$$I_{Plume} = I_{Emitter} - I_{Impinging} \tag{2}$$

$$I_{Target} = I_{Plume} - I_{Secondary} \tag{3}$$

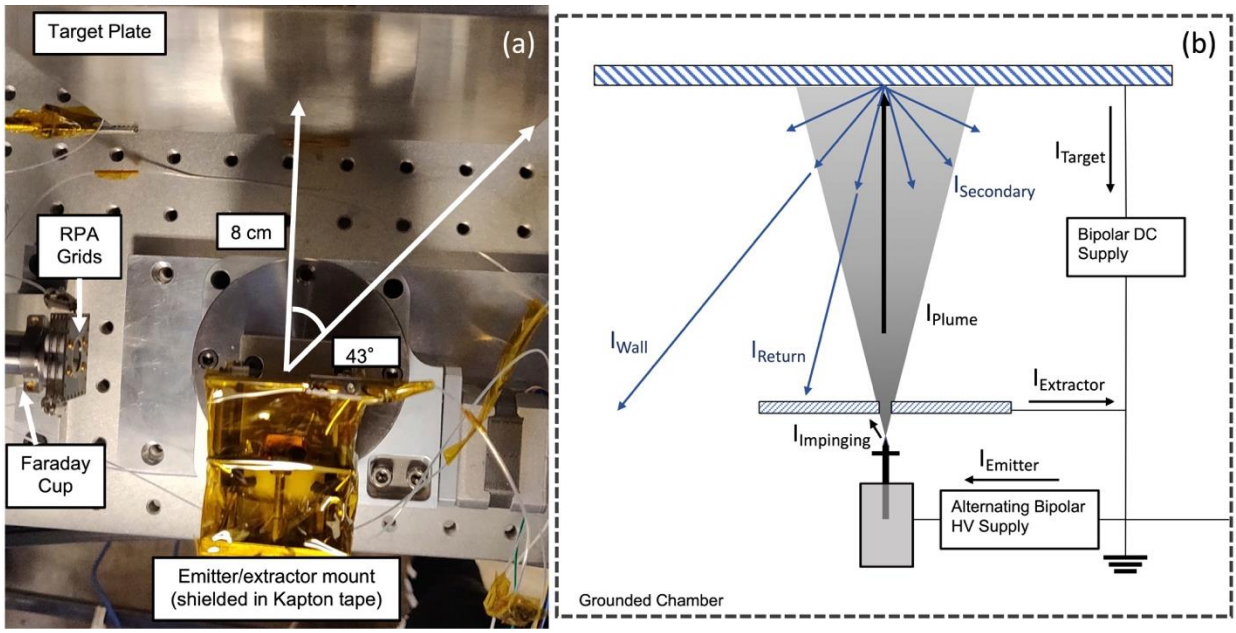

Figure 2: Ion-induced electron emission experimental setup (a) Image of the emitter and target setup in the facility (b) Electrical schematic of the experimental setup

CHAPTER 3

RESULTS

This section describes the results obtained using the experimental setup described above. The performance of the emitter is quantified by emission current, plume current distribution, and plume energy distribution. The surfaces used as targets in the experiments are thoroughly characterized by roughness, composition, and surface layers. Finally, the measured emitter, extractor, and target currents are presented and explained in terms of emitted secondary charges.

Emitter Operation

The performance of the emitter used here (UIUC emitter) is compared in Figure 3 to similar emitters in the literature and in use at Air Force Research Lab (AFRL) Kirtland for [Emim][BF_4] electrosprays.

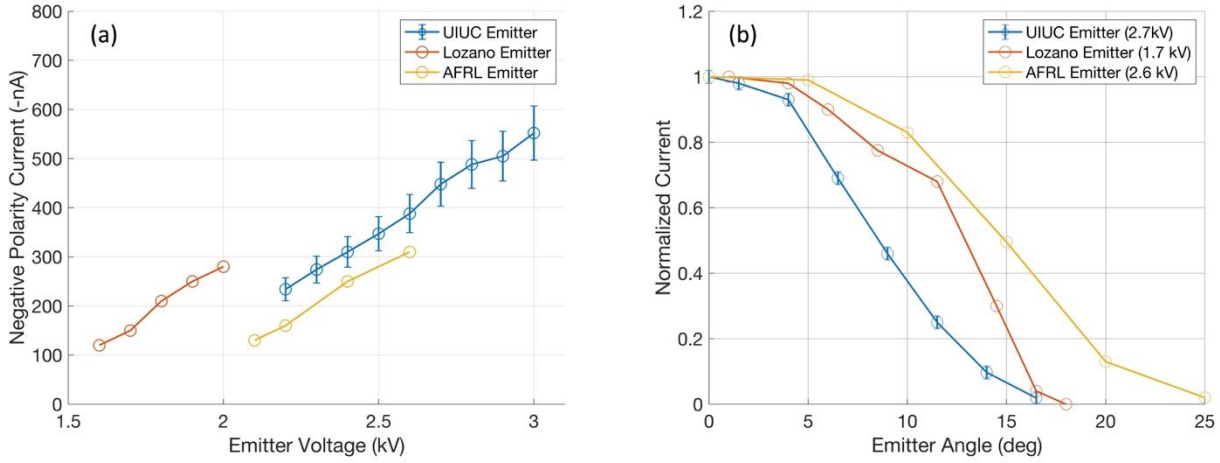

Figure 3: Emitter performance compared to Lozano et. al. [11] and an emitter tested by the author at AFRL Kirtland. (a) Emitter current at different emitter voltages in anion (negative) mode. (b) Plume current angular distribution.

Figure 3a illustrates the measured emitter current in the negative polarity mode. The current linearly increases in magnitude from 200-600 nA for emitter voltages between 2.2-3.0 kV. The

emitter used in these experiments was cleaned, reloaded with IL, and realigned with the extractor between some experiments, resulting in some variation in starting voltage and emitter current. However, the operating voltages stay in the range of 1.5-2.9 kV and emitter currents stay in the range of 200-1000 nA, which is typical in the operation of externally wetted emitters and thrusters [9,11]. Figure 3b illustrates the current density distribution of the electrospray plume and the beam half-cone angle of the emitter used in these experiments is 17°. The measurements for each emitter are normalized by the centerline current density and, although the half-cone angles vary between 17-25°, the angular profile for each emitter follows the same general trend.

An RPA trace at the centerline of the plume and approximately 3 cm from the emitter is shown in Figure 4a. This trace compares well with data in the literature for [Emim][BF_4] plumes from both tungsten wire emitters and porous glass electrospray thrusters [8,9]. In an ideal electrospray plume all ions would be monomers and all ions would be fully accelerated by the extraction potential and the normalized current would drop from 1 to 0 when the retarding potential reaches the extraction potential – at a normalized RPA voltage of 1. Instead, what is illustrated in Figure 4a is that cation and anion dimers are present in the plume, and that dimers fragment into one ion monomer and one neutral pair. If this fragmentation occurs downstream of the extractor, the ion monomer has a kinetic energy proportional to its mass divided by the dimer mass, as calculated in Equation (**4**. This energy level is marked in Figure 4 by the vertical blue and red dashed lines for cations ($0.360V_{Emitter}$) and anions ($0.305V_{Emitter}$), respectively.

$$KE = \frac{m_{monomer}}{m_{dimer}} V_{Emitter} \tag{4}$$

If fragmentation occurs in the acceleration region between the emitter and extractor, the ion monomer is still accelerated by the electric field and has a kinetic energy somewhere between the zero-field fragmentation energy and the total extraction energy. The steady drop in current

denoted “accel-region fragmentation” consists of ions that fragmented at different locations in the acceleration region and suggests that there is an equal probability of fragmentation at all locations between the emitter and extractor. Figure 4b illustrates the derivative of the normalized current in Figure 4a with respect to energy. This yields an approximate energy distribution of the plume with peaks at the “zero-field fragmentation” energy and at the full acceleration energy. The anomalous peak and drop in anion current at retarding potentials less than the zero-field fragmentation energy in Figure 4a is explained as an effect of negative charge emission from the negatively biased RPA grids and is likely not a measure of anion current (our results presented next support this assertion by showing negative charge emission due to anion bombardment significantly increases when a surface is biased negatively). Each of the effects identified in the RPA data of Figure 4 are also reported in the literature [8,9]. While this emitter has not been tested with more advanced diagnostics such as time-of-flight mass spectrometry, we assume based on these favorable comparisons with literature data that the composition of the plume is comparable to other tungsten wire emitters and porous glass electrospray thrusters, which have a plume composition of 40-50% monomers and 50-60% dimers [11,13].

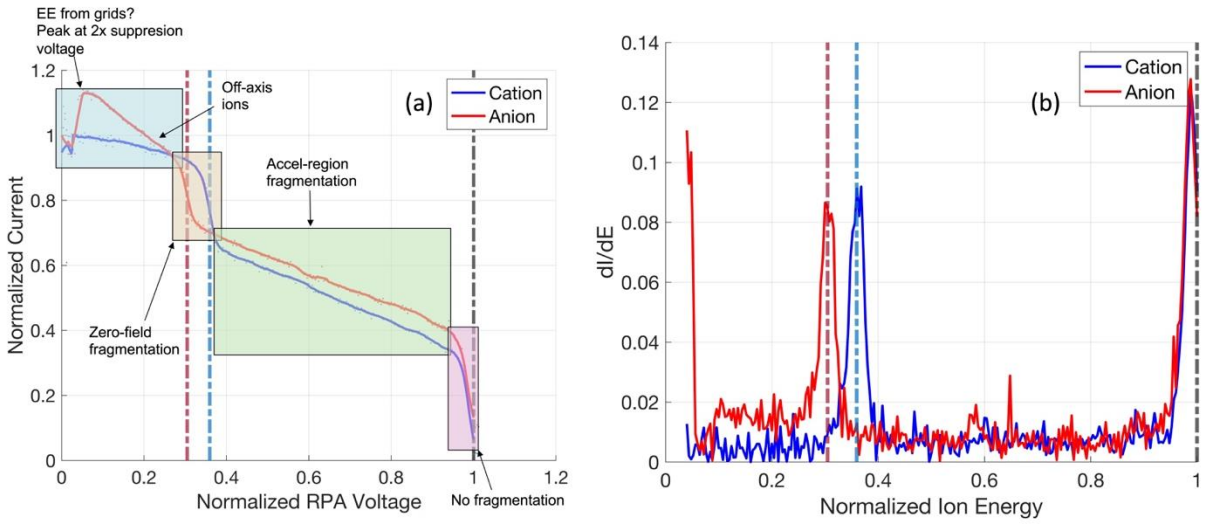

Figure 4: RPA data from the centerline of the plume. (a) Normalized collected current vs. RPA voltage (normalized by emitter voltage). (b) Derivative of normalized current vs. ion energy yields the energy distribution.

Surface Characterization

Eight industrial materials were used in these experiments. 6061 aluminum, carbon graphite, 400 nickel, and 316 stainless steel were selected for their common use in ground-based facilities and thruster/spacecraft construction. Grade 5 titanium, tungsten carbide, and molybdenum were selected for the study of refractory metals. Gold is selected due to its potential as a low sputtering material for coatings on extractor grids or other thruster and spacecraft components. The materials used here are *not* pure sputtering targets but rather commonly used alloys or industrial materials that are found in ground-based test facilities, thrusters, and diagnostics. All materials were purchased from McMaster-Carr and cleaned with water and ethanol, but no other surface modification or treatment was performed. The aluminum, stainless steel, carbon graphite, titanium, and nickel targets are 15x15 cm square plates, the tungsten carbide target is a 7.5x7.5 cm plate, and the gold and molybdenum targets are foils of thickness 25 μm and 127 μm, respectively,

applied to a stainless steel plate. The molybdenum foil covers a 3x3 cm area and the gold foil covers a 2.5x2.5 cm area.

The structure and composition of the material surface or surface layers has the potential to affect the plume-surface interaction properties [14] and therefore it is important to thoroughly characterize both the structure and composition of the surface to better quantify the surface properties. The Keyence VK-X1000 laser microscope at the UIUC Materials Research Laboratory (MRL) is used to take detailed images of the surface and measure the roughness (RMS), average peak height (SPK), and average valley depth (SVK) with an accuracy of 0.5 nm. The equations below explain the calculation of these values which is performed using the Keyence Multi-File Analyzer software.

$$RMS = \sqrt{\frac{1}{l}\int_0^l z(x)^2 dx} \tag{5}$$

$$SPK = \frac{\sum_{i=1}^{n} p_i}{n} \tag{6}$$

$$SVK = \frac{\sum_{i=1}^{n} v_i}{n} \tag{7}$$

where l is the length of the measured area, z(x) is the height of the surface with respect to the mean, p_i is the height of a local maximum on the surface, and v_i is the magnitude of the depth of a local minimum on the surface. The RMS value is a measure of the overall variation in surface height from the mean, while the SPK and SVK values relate to the variation above and below the mean,

respectively, allowing for a distinction between a surface with many craters and one with many ridges.

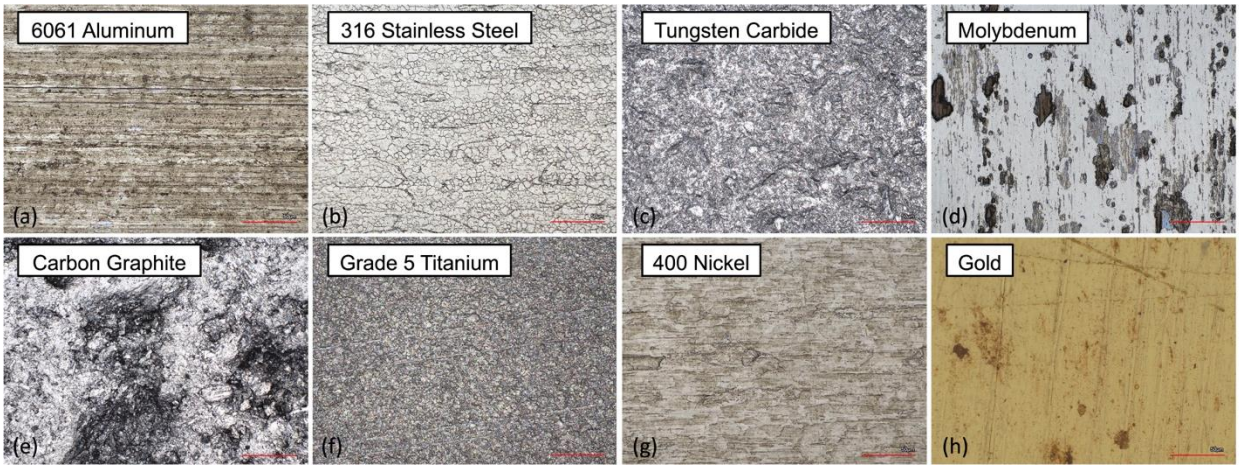

Figure 5: Images of each surface tested in these experiments from the Keyence VK-X1000 laser microscope at 50x magnification. The red scale bar in each image is 50 μm. a) 6061 Aluminum, b) 316 Stainless Steel, c) Tungsten Carbide, d) Molybdenum, e) Carbon Graphite, f) Grade 5 Titanium, g) 400 Nickel h) Gold.

Table 1 displays the surface structure properties measured from each of the images shown in Figure 5. Except for the carbon graphite and tungsten carbide, each of the RMS values fall into the range of 0.1 – 0.5 μm representing relatively smooth surfaces with minor ridges and scratches. The carbon graphite and tungsten carbide have higher RMS values of 4.009 and 1.393 μm, respectively, and both have larger SVK values of 9.184 and 1.763 μm, respectively. The carbon graphite and tungsten carbide have especially rough surfaces with especially large valleys or craters.

Table 1: RMS, SPK, and SVK measurements for each target surface tested in these experiments. The Keyence VK-X1000 has an accuracy of 0.5 nm.

Target Material	Al	SS	Graphite	Ti	WC	Ni	Mo	Au
RMS (μm)	0.393	0.130	4.009	0.283	1.393	0.229	0.448	0.319
SPK (μm)	0.331	0.096	0.998	0.271	0.902	0.171	1.192	0.378
SVK (μm)	0.204	0.236	9.184	0.299	1.763	0.282	0.122	0.269

The Kratos Axis ULTRA x-ray photoelectron spectroscopy (XPS) machine at MRL is used to measure the atomic composition at the surface. XPS is a surface measurement technique that only penetrates a few atomic layers into the sample such that the data are only representative of the surface layer. Data on the tungsten carbide surface could not be collected due to the inability of the XPS machine to pump down to operating pressure because of outgassing from gasses trapped in the material during the manufacturing sintering process.

Table 2: Surface atomic composition (%) of target materials

	Target Material						
Element	Al	SS	C	Ti	Ni	Mo	Au
C	65.24	66.99	65.24	25.42	46.23	24.75	33.18
O	26.74	15.24	26.74	51.06	28.06	50.88	18.28
Al	5.76	---	---	0.54	---	---	---
Fe	---	17.34	---	---	---	---	---
Ti	---	---	---	10.91	2.74	---	---
Ni	---	---	---	---	3.22	---	---
Mo	0.27	---	---	---	---	15.67	---
Au	---	---	---	---	---	---	46.58
Si	---	---	8.02	---	---	2.19	---
Na	1.47	---	---	---	---	6.51	1.95
Zn	1.33	0.43	---	---	5.91	---	---
Mg	9.43	---	---	---	2.16	---	---
V	---	---	---	9.61	---	---	---
Ca	---	---	---	0.25	---	---	---
K	---	---	---	0.92	---	---	---
Cu	---	---	---	---	5.43	---	---
Bi	---	---	---	---	2.44	---	---
Others	< 1	< 0.1	< 0.1	< 0.1	< 2	< 0.1	< 0.1

Additionally, XPS provides measurements of electrons from individual orbitals for each element, allowing for the distinction between metal and metal oxides. Using the XPS energy spectrum and the relative peak heights of metal and metal oxides, and carbon and oxygen, the thickness of the metal oxide layer and the hydrocarbon layer of each surface can be calculated using the method described in Ref. [15]. These results are shown in Table 3. The hydrocarbon layer for each surface ranges from 0.82 nm for molybdenum to 2.71 nm for nickel. These thicknesses are typical of contamination layers for untreated surfaces [15]. Except for titanium, the thicknesses of the oxide layers range from 1.52 nm for nickel to 4.42 nm for molybdenum. Titanium has an oxide layer thickness of nearly twice the thickness of the next largest oxide layer

at 8.63 nm. It is well known that titanium readily oxidizes when exposed to atmosphere [16]**,** which explains why the titanium oxide layer is thicker than the other surfaces.

Table 3: Oxide and hydrocarbon layer thickness of each surface calculated from XPS spectra

Target Material	Al	SS	Graphite	Ti	Ni	Mo	Au
Oxide Layer Thickness (nm)	2.58	3.26	2.35	8.63	1.52	4.42	2.06
Hydrocarbon Layer Thickness (nm)	1.98	2.49	---	0.83	2.71	0.82	1.25

Biased Target Studies

An externally wetted emitter is operated in a 1 Hz AC square wave mode to provide both cation and anion electrospray plumes of [Emim][BF_4]. The currents of the emitter, extractor, and target are measured as the DC bias on the target is increased from -85 V to + 85 V. Figure 6 shows an example of the raw measurements for molybdenum target material. In this example, the externally wetted emitter is operating alternately at ±1.8 kV. The target bias is -85 V. When the emitter voltage is positive, cations are emitted and the emitter current is +450 nA and the target current is +600 nA, which is larger than the emitter current. The extractor current is -100 nA. When the emitter voltage is negative, anions are emitted and the emitter current is -450 nA and the target current is -200 nA, which is more positive than the emitter current. The extractor current is -130 nA. The onset delay and current overshoot when the emitter voltage polarity is switched are typical of externally wetted tungsten emitters and these effects have been characterized by Lozano et. al. [12]. Data like that shown in Figure 6 are collected for several minutes as the target bias is

increased in steps of 5 V every 5 seconds. Each current is averaged for a given operating polarity and target bias voltage. The measurements taken during the onset delay are not included in the averaged currents as the time of the onset delay increases with emitter voltage and varies with the alignment of the emitter and extractor. The averaged currents are plotted as a function of target bias for different target materials and emitter voltages, examples of which are shown in Figure 7.

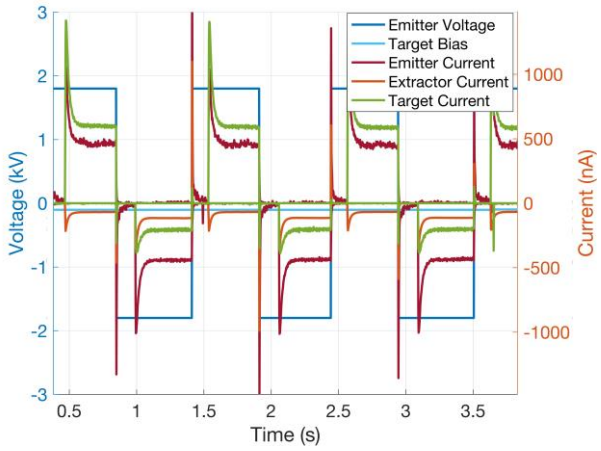

Figure 6: Raw analog signal trace of emitter voltage (blue), emitter current (red), extractor current (orange), target bias (cyan), and target current (green).

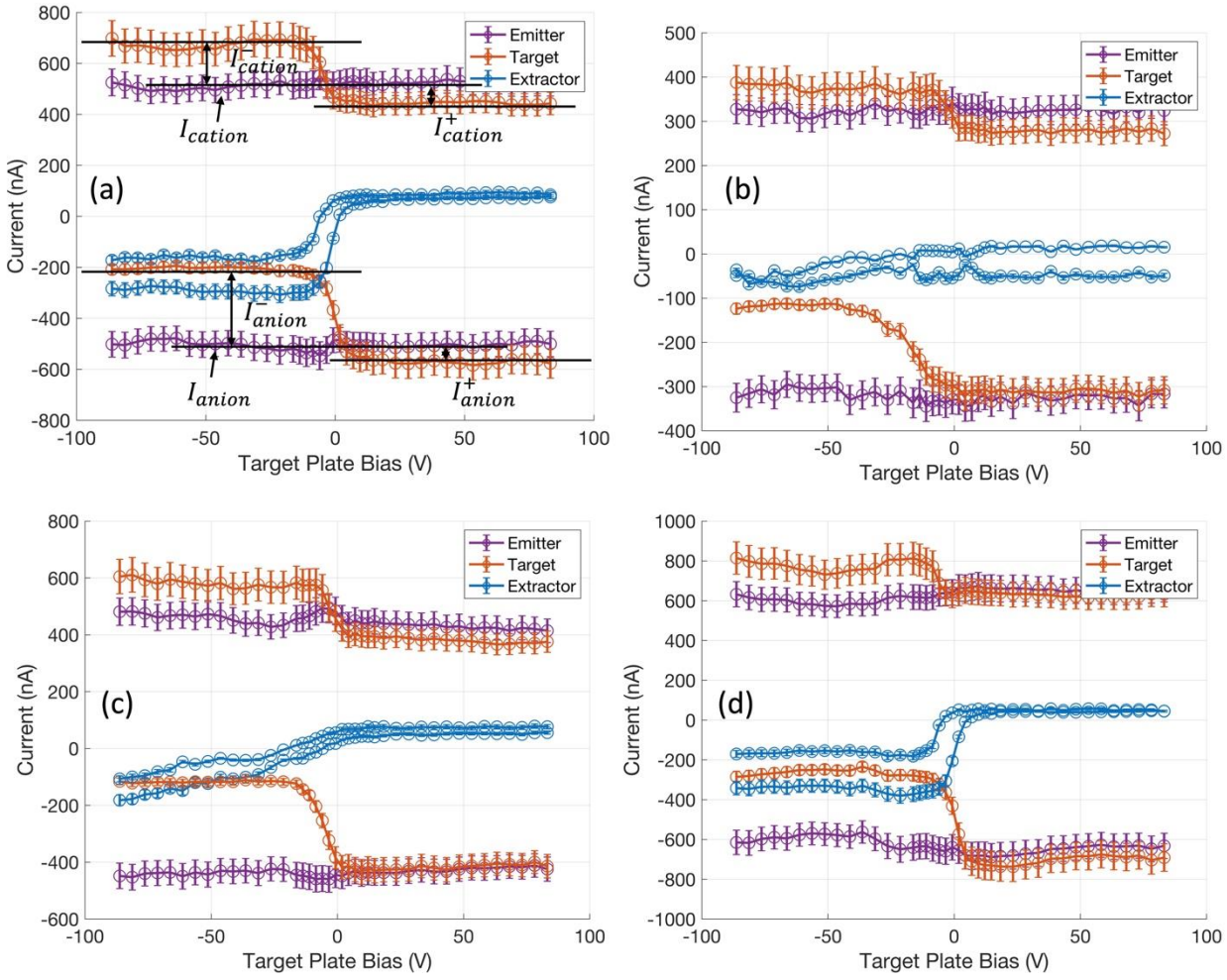

Figure 7: Emitter, extractor, and target currents measured during -85 V to +85 V bias sweep of a) molybdenum target surface at 1.9 kV emitter operating voltage b) aluminum target surface at 1.5 kV emitter operating voltage c) stainless steel target surface at 1.8 kV emitter operating voltage and d) tungsten carbide target surface at 1.9 kV emitter operating voltage

Figure 7 displays measured currents as a function of target bias voltage for some of the target materials and emitter voltages tested. The same general trends are found for all materials although there are quantitative differences that are elaborated on below. Considering Figure 7a, positive currents are collected in the cation operating mode, when the emitter is biased positive. The emitter current is measured at 425-450 nA and does not change with target bias. The target current decreases from 700 nA to 400 nA as the bias on the target increases from -85 V to +85 V.

Negative currents are collected in the anion operating mode when the emitter is biased negative. The emitter current is measured at -425 to -450 nA and does not change with target bias. The target current decreases from roughly -125 nA to -425 nA as the bias on the target is increased from -85 V to +85 V. It is important to note that the target bias of ±85 V is negligible in comparison to the emitter voltages of ≥1.5 kV, and the RPA data in Figure 4 show that very few, if any, ions present in the plume have energies below 85 eV. In other words, the target bias is not repelling or attracting anions or cations emitted by the electrospray emitter.

Still considering Figure 7a, when the target is biased negative, the current measured at the target in both operating polarities is more positive (less negative) than the emitter current. This suggests that at negative target bias there is net negative secondary current being emitted from the surface. This negative secondary current is the difference between the target and emitter currents (assuming negligible extractor impinging current), and we denote it as I^-_{cation} and I^-_{anion} for cation and anion modes, respectively. When the target is biased positive, the current measured at the target in both operating polarities is more negative (less positive) than the emitter current. This suggests that at positive target bias there is net positive secondary current being emitted from the surface. This positive secondary current is the difference between the target and emitter currents and we denote it as I^+_{cation} and I^+_{anion} for cation and anion modes, respectively. While we have focused this description of the results on Figure 7a, the same general trends can be seen in Figure 7b, c, and d, and are present for all materials and all emitter voltages tested.

For each Figure 7a-d, and in all experiments performed, the cation mode extractor current is more positive (less negative) than the anion mode extractor current. The extractor current in Figure 7a increases from -180 nA to 80 nA in cation mode and -280 nA to 80 nA in anion mode. This change in extractor current is attributed to the collection of emitted charges from the target

surface. Secondary emitted charge from the biased target is travelling upstream and being collected at the grounded extractor.

Figure 8a shows the difference between the secondary current emitted from the target and the current measured at the extractor as a percentage of emitter current averaged over all tests of the targets at 1 cm distance and 8 cm distance. The percent difference is calculated as shown in Equation (**8**) for the ± 85 V point in each cation and anion mode. For the targets tested where the target distance from the extractor is only 1 cm (tungsten carbide, molybdenum, and gold), the extractor current matches the target secondary emission current within 8% for both polarity modes and for both negative and positive target biases. For the surfaces tested where the distance from the extractor is 8 cm, these currents do not match nearly as well and are very inconsistent, with discrepancies up to 40%. This is also illustrated in Figure 7b-c where the changes in extractor current do not track as closely with the changes in target current. As illustrated in Figure 8a, the percent difference for 8 cm targets is much larger for negative secondary charges than for positive secondary charges. This could be due to a difference in trajectory and mobility in electrons vs ions. While the composition of positive secondary charges inherently must be all ions, the composition of negative secondary charges could be a mix of ions and electrons. These results suggest electrons are less likely to travel back to the extractor than positive ions.

$$Percent\ Difference = 100 \times \frac{\left|I_{Secondary}\right| - |I_{Extractor}|}{|I_{Emitter}|} \tag{8}$$

When the distance of the target from the extractor is increased even further (> 8 cm), it is even less likely that the secondary emission current travels directly upstream to the grounded extractor. To further verify the presence of return current, the electrospray plume was pointed away from any nearby targets or diagnostics such that emitted ions would impinge upon the grounded

chamber surface 61 cm away. Figure 8b shows an example data set for this configuration. The extractor current is below ± 30 nA while the emitter current is ± 700 nA. In this configuration, the extractor current is measured to be at all times less than 5% of the emitter current and is always the same polarity as the emitter current, suggesting this extractor current is due to emitted ions from the emitter impinging on the extractor ($I_{Impinging}$) and not due to secondary emission charge from the far downstream surface.

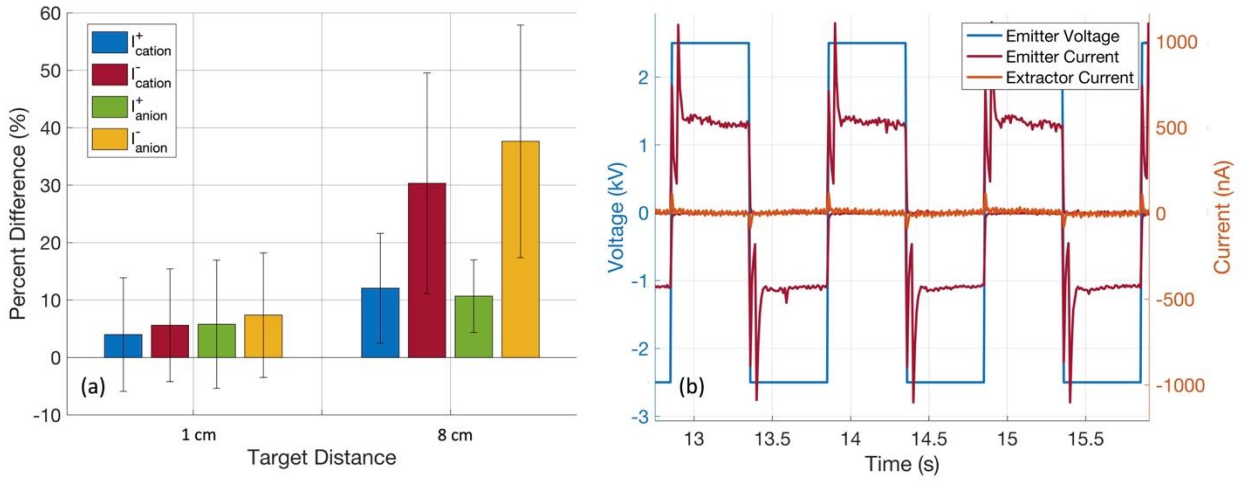

Figure 8: a) Percent difference between the secondary current emitted and the current measured at the extractor as a percentage of emitter current for 1 cm and 8 cm distance targets b) Raw analog signal trace of emitter voltage (blue), emitter current (red), and extractor current (orange) while the emitter plume is aimed away from any nearby surfaces.

CHAPTER 4

ANALYSIS AND DISCUSSION

Secondary Charge Emission Yield

The data presented in Figure 7 can be interpreted as the secondary charge emission yield from a given target material. The emission yield can be calculated using the experimental data by dividing the magnitude of the secondary current by the magnitude of the plume current ($I_{Plume} \approx I_{Emitter}$). Given the steady-state behavior at both ends of the target bias range in Figure 7 and the typical energy of secondary electrons and ions from Ar^+ bombardment of materials are typically only a few eV [17,18], it is unlikely that any emitted charges of the opposite polarity remain unsuppressed at the ± 85 V target bias. There are two electrospray operating modes (cation, anion) and two possible types of emitted current (positive, negative), so there are four yields calculated using Equations 10-13: yield of positive charges per incident cation (γ^+_{cation}), yield of negative charges per incident cation (γ^-_{cation}), yield of positive charges per incident anion (γ^+_{anion}), and yield of negative charges per incident anion (γ^-_{anion}).

$$Charge\ Yield = \gamma = \frac{|I_{Secondary}|}{|I_{Plume}|} \tag{9}$$

$$\gamma^+_{cation} = \frac{|I^+_{cation}|}{|I_{emitter,c}|} \tag{10}$$

$$\gamma^-_{cation} = \frac{|I^-_{cation}|}{|I_{emitter,c}|} \tag{11}$$

$$\gamma^+_{anion} = \frac{|I^+_{anion}|}{|I_{emitter,a}|} \tag{12}$$

$$\gamma^{-}_{anion} = \frac{|I^{-}_{anion}|}{|I_{emitter,a}|} \tag{13}$$

where $I_{emitter,c}$ is the emitter current measured in cation mode and $I_{emitter,a}$ is the emitter current measured in anion mode. These yields are calculated and presented in Figure 9 for each target material tested over a range of emitter operating voltages from 1.5 to 2.9 kV.

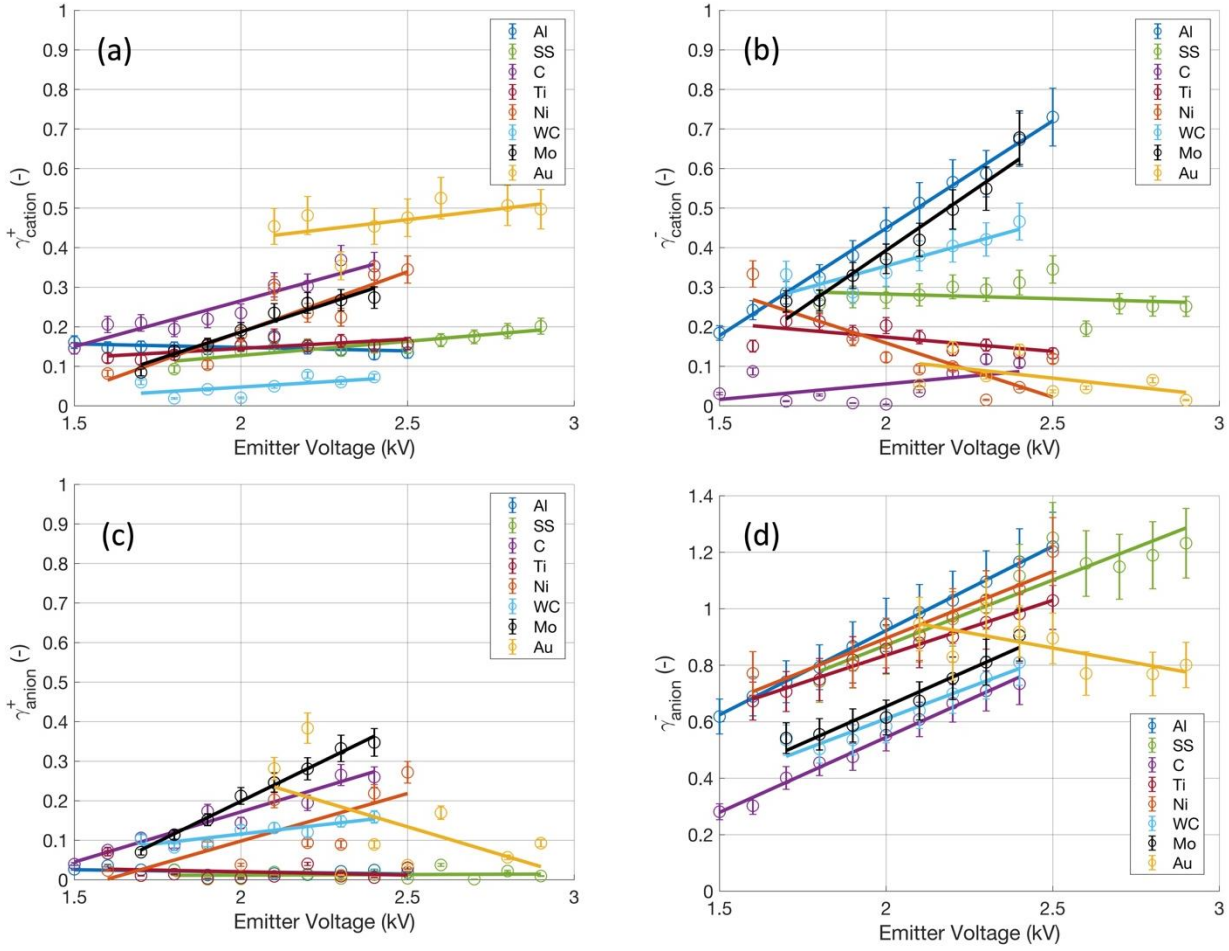

Figure 9: Calculated yields of secondary charge per incident ion of each material for a) positive charge per incident cation b) negative charge per incident cation c) positive charge per incident anion and d) negative charge per incident anion for different emitter operating voltages from 1.5 to 2.9 kV

The yields for most materials illustrated in Figure 9 exhibit a linearly increasing yield with increasing emitter voltage for all four emission yields. γ^{+}_{cation} ranges from roughly 0.05 for

molybdenum to 0.55 for gold with all other materials falling somewhere in between. γ^{-}_{cation} ranges from roughly 0.05 at the low end of the carbon graphite, nickel, and gold materials to 0.7 at the high end of the aluminum yield data. γ^{+}_{anion} ranges from 0 for nickel, titanium, and stainless steel to 0.4 for gold, although the yield for gold decreases greatly as the emitter voltage increases. Molybdenum, however, reaches 0.35 at large emitter voltages and exhibits a faster linear increase with emitter voltage with a slope of 0.4 kV^{-1} whereas gold displays a linearly decreasing trend suggesting that molybdenum would have the highest value of γ^{+}_{anion} as emitter voltage continues to increase. γ^{-}_{anion} exhibits by far the largest yields ranging from 0.3 at the low end of carbon graphite to nearly 1.3 at the high end of aluminum and stainless steel. For negative secondary charges carbon graphite, molybdenum, and gold display among the highest yields in both cation and anion plumes and aluminum, titanium, and stainless steel display among the lowest in both cation and anion plumes. For positive secondary charges aluminum displays the highest yields and carbon graphite displays the lowest yields in both cation and anion plumes.

Surface oxide and hydrocarbon layers are known to affect secondary charge emissions. However, a comparison of the yields with surface layer thickness for the different materials did not show any clear trend or correlation. Future work should make a comparison between targets of the same material with different layer thicknesses to study the effect of oxide and hydrocarbon surface layers more directly.

The experimental implications of the data presented in Figure 9 are that secondary charge emission from surfaces bombarded by electrospray plumes is unavoidable by applying a bias in either polarity to the surface. For example, a tungsten carbide surface could be used for charge collection in a cation plume and be positively biased to suppress emission of negative charges from the surface (γ^{-}_{cation}), but the measured current will still need to be adjusted by 5-10% to account

for the emission of positive charges from the surface (γ^{+}_{cation}) depending on the emitter voltage. Using the current vs. target bias traces in Figure 7, a surface could be biased at the point where the target current is equal to the emitter current. However, this is not necessarily the point where there is no secondary charge emission, but rather there could be equal positive and negative secondary charge being emitted and this cannot be determined without further characterization of the secondary charges at different target biases. Additionally, most electrospray diagnostics involve more complicated systems than a single charge collecting plate and one electrospray operating polarity. Often, as in these experiments, the emitter or thruster is operated in an alternating polarity mode and most diagnostics include additional biased surfaces, grids, and other components which may be subject to impingement from the plume. Even with proper experimental design, it will quickly become difficult to verify the source of the currents being collected. This challenge would be greatly eased by the development of higher fidelity electrospray modelling which utilizes secondary charge yield data to model an experimental system or thruster-spacecraft configuration more accurately.

Figure 10 illustrates the negative secondary charge emission yields of an [Emim][BF_4] electrospray plume versus ion-induced electron emission (IIEE) from a Xe^+ ion beam for aluminum, molybdenum, and gold surfaces [19–22]. For aluminum, the yields of [Emim][BF_4] cations and anions increase from 0.2-0.75 and 0.6-1.2, respectively, over the 1.5-2.5 kV emitter voltage range. For molybdenum, the yields of [Emim][BF_4] cations and anions increase from 0.25-0.7 and 0.55-0.9, respectively, over the 1.7-2.4 kV emitter voltage range. For gold, the yields of [Emim][BF_4] cations and anions range from 0-0.15 and 0.75-1, respectively, over the 2.1-2.9 kV emitter voltage range. Xenon requires much higher ion energies to induce negative charge emission with the yield reaching 0.1 at 4-5 keV and increasing to 1 at 23-42 keV for all three

materials. Figure 10 clearly illustrates that, at least for aluminum, molybdenum, and gold, the negative charge emission is more significant at lower energy for electrospray plumes than for electric propulsion systems utilizing xenon propellant.

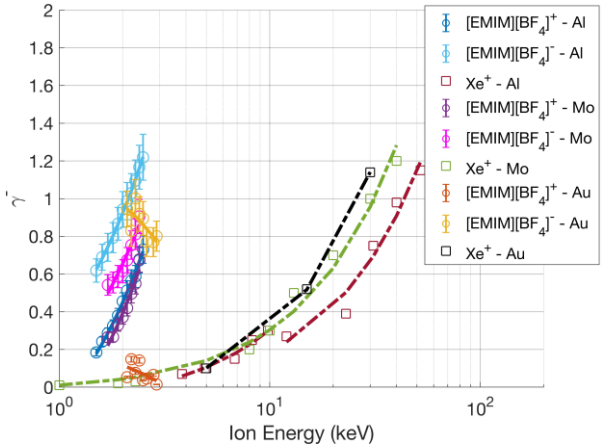

Figure 10: Negative charge yields of [Emim][BF_4] electrospray plumes compared with ion-induced electron emission caused by xenon ion beam [19–22].

As discussed earlier, previous studies involving charge emission from surfaces bombarded by electrospray plumes have focused on IIEE caused by impinging cations. The evidence of positive charge emission presented in Figure 7 and Figure 9 strongly suggests that electrons are not the only charged particles emitted from surfaces bombarded by electrospray plumes and possibly not the only negative charges emitted. It is also clear that charge emission is an equally important consideration for anion plumes. The following sections will explore previous work on IIEE in electrosprays as it relates to the data presented here and the feasibility of ions being emitted from surfaces bombarded by electrospray plumes.

Target Bias for Net Zero Secondary Current

In an ideal system without secondary charge emission, the current measured at the target would be equal to the current measured at the emitter (assuming negligible current to the extractor).

Due to secondary charge emission, however, the current measured at even a grounded target is likely to deviate from the total electrospray plume current impinging on the surface. Figure 11a illustrates the target bias voltage required such that there is zero net secondary current for cation (blue) and anion (red) mode. This target bias voltage is denoted the zero point. While the net secondary current is zero this does not necessarily mean there is no secondary charge emission, as there could be equal quantities of positive and negative secondary charges being emitted from the surface. For all materials tested the zero point voltage is in the range of ±10 V. For all materials in anion mode the zero point is at a positive target bias from 2.5-9 V and for all materials in cation mode the zero point is at a negative target bias from negative 1-8.5 V, except for nickel which has a cation mode zero point of +0.5 V. The error bars on these measurements represent one standard deviation in each direction of the zero points for the set of measurements collected at each emitter voltage.

Target Bias for Full Suppression of Opposite Polarity Charge Emission

Applying a bias to the target in either polarity suppresses the emission of secondary charges of the opposite polarity. As Figure 7 shows, as the target bias magnitude is increased, the magnitude of the current measured at the target plateaus and reaches a steady-state. This constant target current indicates full suppression of opposite polarity charge emission and that there is only secondary emission of charges in the same polarity of the target bias. We define the target bias voltage at which the target current becomes < 5% of its steady state as the bias voltage for full suppression of opposite polarity charge emission. Using the data of Figure 7 for all test cases, the full suppression bias voltage is calculated for each positive and negative target bias in cation and anion modes, and is averaged over all emitter voltages tested. The target bias for full suppression of opposite polarity charge emission is plotted for each material in Figure 11b. Generally, a target

bias of < ±20 V is required to reach full suppression. However, the aluminum surface requires -58 V for a negative target bias in anion mode. It is unclear why a much larger target bias is required for full suppression in this instance. The error bars on these measurements represent one standard deviation for the set of measurements collected at each emitter voltage.

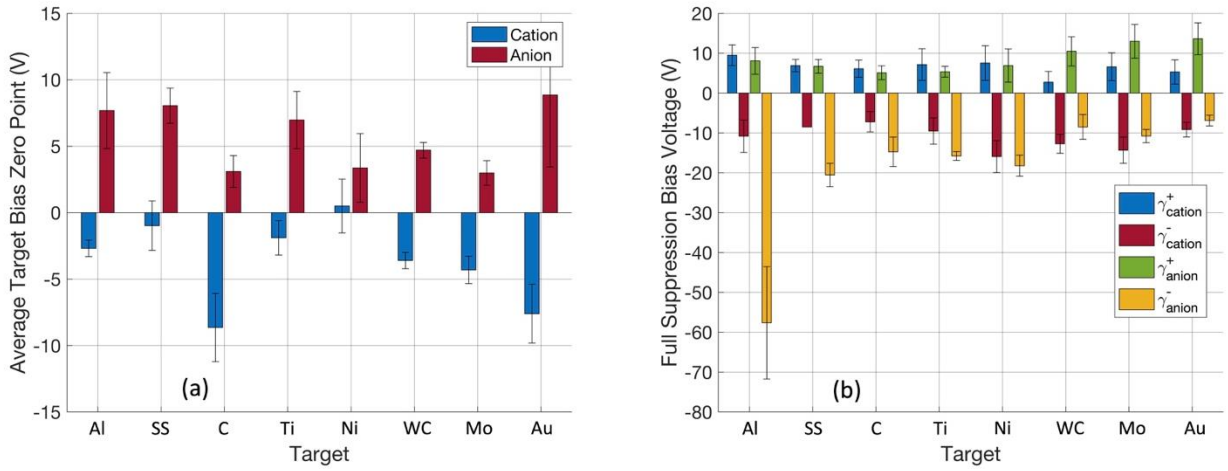

Figure 11: a) The target bias voltage at which the net secondary emission current is zero b) The target bias voltage for full suppression of opposite polarity charge emission.

Ion-Induced Electron Emission

The primary mechanism of charge emission considered in the literature is ion-induced electron emission (IIEE), where a high energy primary ion impinging on a surface results in an electron being emitted from the surface. This process is primarily attributed to the mechanism of kinetic electron emission (KEE), where some of the kinetic energy of the incident ion is transferred to the electron and causes it to migrate to and then leave the surface. A more detailed explanation of electron emission mechanisms can be found in [17]. The data presented in this work is compared in this section to existing theoretical and experimental data focusing on IIEE.

Recent work by Magnusson et. al. in modelling electron emission from incident polyatomic ions using the software TRansport of Ions in Matter (TRIM) has been applied to $Emim^+$ monomer

ions. Figure 12a compares this theoretical dataset to the data presented in Figure 9b for the negative charge yield of a cation plume impinging on a stainless steel target. The theoretical work assumes a monoenergetic, single species ion beam impinging on a pristine stainless steel surface. The theoretical yields (UCLA, orange) increase from 1.2-1.9 over the ion energy range of 1.6-2.8 keV, and are on the order of 6-9 times larger than the experimentally measured yields (UIUC). Further, the theoretical predictions display an increasing trend with emitter voltage while the experimental results are constant.

Closer agreement is obtained when one considers the ion energy distribution of the experimental plume is not monoenergetic. The theoretical yields are modified based on the energy distribution of Figure 4. This adjustment is done by numerically integrating the change in normalized current in Figure 4a multiplied by the emission yield energy distribution of the unadjusted data in orange (UCLA) as shown in Equation (**14**).

$$\gamma_{adj}(V_{Emitter}) = \int_0^{V_{Emitter}} -\frac{dI_{Norm}}{dE}\gamma_{theo}dE \tag{14}$$

Where γ_{adj} is the adjusted electron emission yield as a function of emitter voltage, I_{Norm} is the normalized current of the RPA measurement, γ_{theo} is the theoretical electron emission yield as a function of energy, and E is the energy of the impinging ion. The data presented in red in Figure 12a (UCLA-Adj) is the result. The adjusted emission yield increases from 0.8-1.2 over an energy range of 1.8-2.9 keV, and is still 3-4x larger than the experimental measurements and still displays an increasing trend. These remaining differences may be because the experimental plume consists not just of monomers, but also of dimers and neutrals (resulting from fragmented dimers) and that the real surfaces have finite thickness oxide and hydrocarbon surface layers.

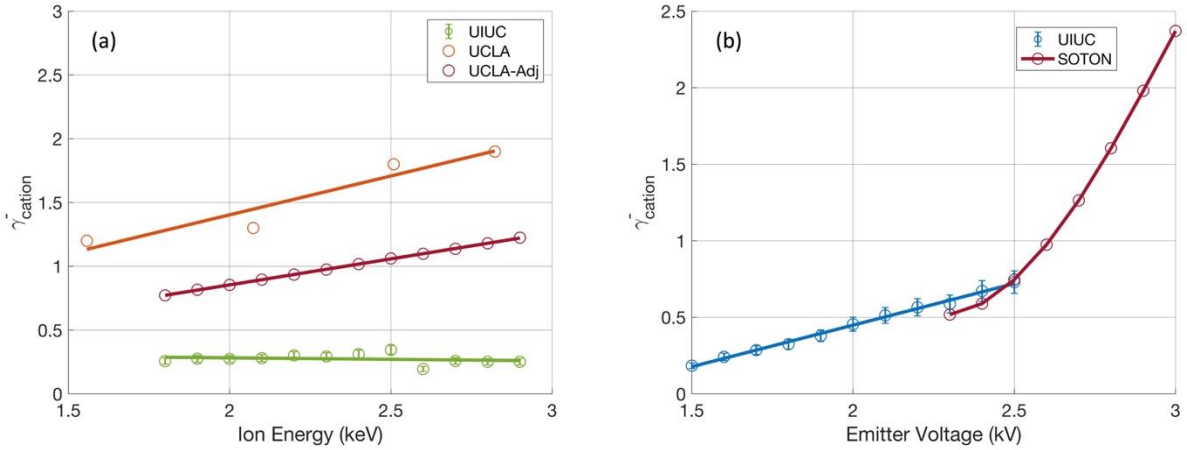

Figure 12: Comparison of a) negative charge yield of stainless steel compared to theoretical calculations in [10] and adjusted for plume energy distribution and b) negative charge yield of aluminum compared to experimental data from a porous glass electrospray thruster in [9].

Figure 12b compares the experimental data presented in Figure 9b of the negative charge yield of a cation plume impinging on an aluminum surface to a similar measurement performed utilizing a porous glass electrospray thruster at University of Southampton (SOTON) [9]. This experiment was intended to suppress IIEE, but is interpreted here as the suppression of all negative charges from the surface. In the experiment performed at SOTON, a nickel mesh grid is positioned in front of the aluminum current collecting surface and biased negative to suppress the emission of negative charges from the aluminum surface similar to how we bias the surface itself positive in these experiments. The difference in current collected between the 0 V grid bias and bias voltage required to fully suppress secondary charge emission (-60-80 V) is used to calculate the negative charge emission yield for impinging cations as shown in Equation 7. The negative secondary emission yield from University of Southampton increases from 0.5-2.4 over a range of emitter voltages from 2.3-3 kV. While a more complete overlap of energy range is needed to make a full comparison between datasets, the experimental data presented in this paper agrees well in the very narrow emitter voltage range of 2.3-2.5 kV, with yields in both datasets increasing from

approximately 0.55-0.75. The combination of UIUC and SOTON data in Figure 12b suggests a change in slope of the emission yield for aluminum at about 2.5 kV, but this has not been verified within a single experiment. The anion mode data collected from SOTON does not agree with the results collected here. When the nickel mesh grid is biased negatively in anion mode, no change in the collected current was observed, which suggests a negative secondary charge yield of 0 for impinging anions, whereas in Figure 9d the negative secondary charge yield for anions impinging on aluminum ranges from 0.6-1.2. It may be that due to the higher current density of a porous glass electrospray thruster, the space-charge effect of the negatively charged plume suppresses negative secondary charges from being emitted from the surface.

Secondary Ion Emission

The previous section discussed work in electrospray charge emission that has assumed IIEE is the only form of charge emission from surfaces. The data presented in Figure 7 and Figure 9 illustrates a more complicated picture of charge emission in electrospray plume-surface interactions. The existence of the positive charge emission yields and their dependence on emitter voltage strongly suggests that positive ions are being emitted from the surface and prompts the possibility that negative ions may be emitted from the surface along with electrons. The experiments performed in this work do not allow for a distinction between different species of the same charge emitted from the surface. It is well known through the study of technologies such as time-of-flight secondary ion mass spectrometry (TOF-SIMS) that in addition to sputtered neutral particles, positive and negative ions can be sputtered from surfaces. Lundquist et. al. [18] find that secondary cations contribute 50% of sputtered species from pure copper bombarded by a 3 keV Ar^+ beam and emission of secondary cations from pure surfaces is much more common than emission of secondary anions [18,23,24]. However, sputtering of the oxide layer of aluminum at

incident ion energies below 500 eV has been shown to result in O^- yields of similar magnitude to the electron emission yield [14]. Gries et. al. [25] find that secondary cations contribute 10% of sputtered species from pure aluminum sputtered by a 5 keV Ar^+ beam. While the sputtering mechanisms would certainly be different for an electrospray plume, it is possible that secondary ions contribute to the secondary current measured in Figure 7.

Another complication of these experiments with [Emim][BF_4] plumes is that the IL condenses and builds up into a thin film on the surface [10,26]. The time dependence of this buildup has yet to be studied. It is reasonable to assume that such an IL thin film would itself be sputtered by the electrospray plume and result in charged propellant ions or droplets being emitted from the surface. Each target surface tested here is impinged upon by the electrospray plume for approximately one hour. If every ion incident on the surface contributed to an evenly distributed IL layer, based on the 17º plume divergence, it would result in a 1.6 nm layer by the end of an experiment with an 8 cm distance between the emitter and target, and a 98.9 nm layer for a 1 cm distance between the emitter and target. In experiments, these thicknesses would vary from larger thicknesses in the center of the plume and smaller thicknesses as the angle from the center increases. Layers of this order of thickness could entirely change the plume-surface interaction to a point where the plume is no longer interacting with the target surface itself. However, we observe that the secondary charge yield is different for each surface studied, so it is unlikely that if an IL thin film is created it reaches thicknesses where the plume no longer interacts with the surface. More experimental data is needed to determine how IL thin films accumulate and how this mechanism could affect the secondary charge emission properties.

CHAPTER 5

CONCLUSION

Emitted secondary charge yields have been measured for eight different materials bombarded by [Emim][BF_4] electrospray plumes for emitter voltages between 1.5-2.9 kV. We find that positive and negative secondary charge can be emitted from a surface bombarded by cations and anions. The secondary positive charge yield during cation bombardment (γ^+_{cation}) ranges from 0-0.55, the secondary negative charge yield during cation bombardment (γ^-_{cation}) ranges from 0-0.75, the secondary positive charge yield during anion bombardment (γ^+_{anion}) ranges from 0-0.4, and the secondary negative charge yield during anion bombardment (γ^-_{anion}) ranges from 0.3-1.3. While common interpretation in the literature suggests that ion-induced *electron* emission is the only important charge emission mechanism, evidence is presented here supporting the possibility of sputtered ions. The yields presented here should be used by experimentalists to inform material choice and experimental design and correct current measurements in experiments. These yields and future work in this area should be used by modelling groups to develop high fidelity electrospray models capable of predicting facility effects in experiments and more accurately predicting thruster performance and thruster-spacecraft interactions. Future experimental work in this area should measure energy and mass distributions of emitted electrons and ions to better characterize the plume-surface interaction and should also filter the electrospray plume by energy and mass to measure the charge emission yields dependence on incident energy and species. Experiments should also characterize IL accumulation on surfaces and the effect an IL layer has on sputtering and secondary charge emission.

REFERENCES

[1] Krejci, D., and Lozano, P. "Scalable Ionic Liquid Electrospray Thrusters for Nanosatellites." *Advances in the Astronautical Sciences*, Vol. 157, No. February, 2016, pp. 801–810.

[2] Ma, C., and Ryan, C. N. "The Design and Characterization of a Porous-Emitter Electrospray Thruster (PET-100) for Interplanetary CubeSats." *Proceeding of the 7th Interplanetary CubeSat Workshop*, No. May, 2018, pp. 1–9.

[3] Natisin, M. R., Zamora, H. L., McGehee, W. A., Arnold, N. I., Holley, Z. A., Holmes, M. R., and Eckhardt, D. "Fabrication and Characterization of a Fully Conventionally Machined, High-Performance Porous-Media Electrospray Thruster." *Journal of Micromechanics and Microengineering*, Vol. 30, No. 11, 2020, p. 115021. doi:10.1088/1361-6439/abb8c3.

[4] Saiz, F., and Gamero-Castaño, M. "Molecular Dynamics of Nanodroplet Impact: The Effect of the Projectile's Molecular Mass on Sputtering." *AIP Advances*, Vol. 6, No. 6, 2016. doi:10.1063/1.4954740.

[5] Perez-Martinez, C., Guilet, S., Gogneau, N., Jegou, P., Gierak, J., and Lozano, P. "Development of Ion Sources from Ionic Liquids for Microfabrication." *Journal of Vacuum Science & Technology B, Nanotechnology and Microelectronics: Materials, Processing, Measurement, and Phenomena*, Vol. 28, No. 3, 2010, pp. L25–L27. doi:10.1116/1.3432125.

[6] Villanueva-Bonay, E., and Gamero-Castaño, M. "Molecular Dynamics of Nanodroplet Impact: The Effect of Particle Resolution in the Projectile Model." *AIP Advances*, Vol. 9, No. 8, 2019. doi:10.1063/1.5100964.

[7] Mier-Hicks, F., and Lozano, P. C. "Spacecraft-Charging Characteristics Induced by the

Operation of Electrospray Thrusters." *Journal of Propulsion and Power*, Vol. 33, No. 2, 2017, pp. 456–467. doi:10.2514/1.B36292.

[8] Coles, T. M., Fedkiwf, T. P., and Lozano, P. C. "Investigating Ion Fragmentation in Electrospray Thruster Beams." *48th AIAA/ASME/SAE/ASEE Joint Propulsion Conference and Exhibit 2012*, No. August, 2012. doi:10.2514/6.2012-3793.

[9] Ma, C., and Ryan, C. "Plume Characterization of a Porous Electrospray Thruster." *The 36th International Electric Propulsion Conference*, 2019, pp. 1–19.

[10] Magnusson, J. M., Collins, A. L., and Wirz, R. E. "Polyatomic Ion-Induced Electron Emission (Iiee) in Electrospray Thrusters." *Aerospace*, Vol. 7, No. 11, 2020, pp. 1–21. doi:10.3390/aerospace7110153.

[11] Lozano, P., and Martínez-Sánchez, M. "Ionic Liquid Ion Sources: Characterization of Externally Wetted Emitters." *Journal of Colloid and Interface Science*, Vol. 282, No. 2, 2005, pp. 415–421. doi:10.1016/j.jcis.2004.08.132.

[12] Lozano, P., and Martínez-Sánchez, M. "On the Dynamic Response of Externally Wetted Ionic Liquid Ion Sources." *Journal of Physics D: Applied Physics*, Vol. 38, No. 14, 2005, pp. 2371–2377. doi:10.1088/0022-3727/38/14/011.

[13] Petro, E. M., Bruno, A. R., Lozano, P. C., Perna, L. E., and Freeman, D. S. "Characterization of the Tile Electrospray Emitters." *AIAA Propulsion and Energy 2020 Forum*, 2020, pp. 1–13. doi:10.2514/6.2020-3612.

[14] Tucek, J. C., and Champion, R. L. "On the Dynamics of Secondary-Electron and Anion Emission from an Al/O Surface." *Surface Science*, Vol. 382, No. 1–3, 1997, pp. 137–146. doi:10.1016/S0039-6028(97)00117-9.

[15] Klingner, S., Voigts, F., Viöl, W., and Maus-Friedrichs, W. "Analysis of Plasma Degreased

Aluminium Foil with XPS." *Surface Engineering*, Vol. 29, No. 5, 2013, pp. 396–401. doi:10.1179/1743294413Y.0000000129.

[16] Zhang, Y., Fang, Z. Z., Xu, L., Sun, P., Van Devener, B., Zheng, S., Xia, Y., Li, P., and Zhang, Y. "Mitigation of the Surface Oxidation of Titanium by Hydrogen." *Journal of Physical Chemistry C*, Vol. 122, No. 36, 2018, pp. 20691–20700. doi:10.1021/acs.jpcc.8b04684.

[17] Delpa, D., and Mahieu, S. *Reactive Sputter Deposition*. 2008.

[18] Lundquist, T. R. "Energy Distributions of Sputtered Copper Neutrals and Ions." *Journal of vacuum science & technology*, Vol. 15, 1998.

[19] Alonso, E. V., Baragiola, R. A., Ferrn, J., Jakas, M. M., and Oliva-Florio, A. "Z1 Dependence of Ion-Induced Electron Emission from Aluminum." *Physical Review B*, Vol. 22, No. 1, 1980, pp. 80–87. doi:10.1103/PhysRevB.22.80.

[20] Svensson, B., Holmén, G., and Burén, A. "Angular Dependence of the Ion-Induced Secondary-Electron Yield from Solids." *Physical Review B*, Vol. 24, No. 7, 1981, pp. 3749–3755. doi:10.1103/PhysRevB.24.3749.

[21] Ferron, J., Alonso, E. V., Baragiola, R. A., and Oliva-Florio, A. "Electron Emission from Molybdenum under Ion Bombardment." *Journal of Physics D: Applied Physics*, 1981.

[22] Ferron, J., Alonso, E. V., Baragiola, R. A., and Oliva-Florio, A. "Dependence of Ion-Electron Emission from Clean Metals on the Incidence Angle of the Projectile." Vol. 24, No. 8, 1981, pp. 4412–4419.

[23] Wittmaack, K. "Analysis of Quantitative Secondary Ion Mass Spectrometry." *Nuclear Instruments and Methods*, Vol. 168, 1980.

[24] Jurela, Z. "Energy Distribution of Secondary Ions From 15 Polycrystalline Targets."

Radiation Effects, Vol. 19, No. 3, 1973, pp. 175–180. doi:10.1080/00337577308232239.

[25] Gries, W. H. "A Formula for the Secondary Ion Field Fraction Emitted Through and Energy Window." *International Journal of Mass Spectrometry and Ion Physics*, Vol. 17, 1975, pp. 77–88.

[26] Ma, C. (University of S. *Design and Characterization of Electrospray Thrusters with High Emission Density*. University of Southampton, 2020.

[27] Chakraborty, S., Courtney, D. G., and Shea, H. "A 10 NN Resolution Thrust-Stand for Micro-Propulsion Devices." *Review of Scientific Instruments*, Vol. 86, No. 11, 2015. doi:10.1063/1.4935471.

[28] Chakraborty, S. *An Electrostatic Ion-Guide and a High-Resolution Thrust-Stand for Characterization of Micro-Propulsion Devices*. 2015.

APPENDIX A

FULL COLLECTION OF CURRENT VS. TARGET BIAS PLOTS

Aluminum

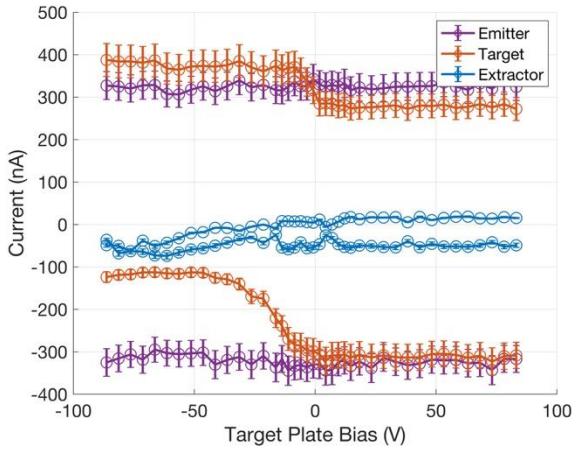

1.5 kV

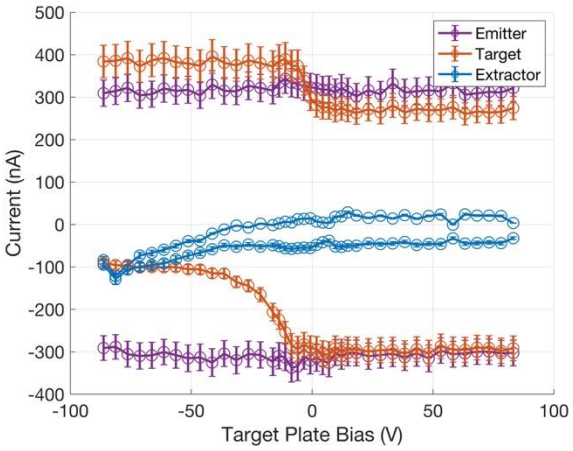

1.6 kV

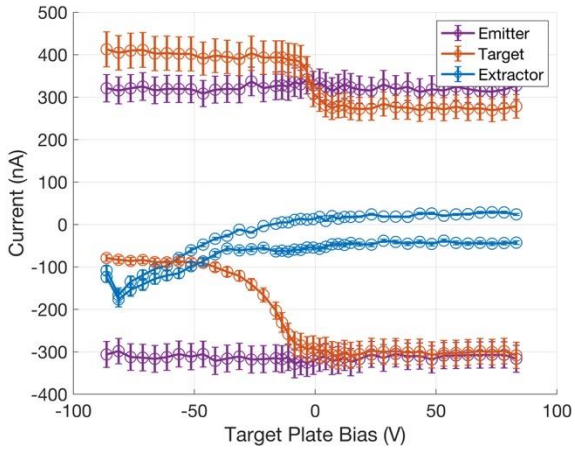

1.7 kV

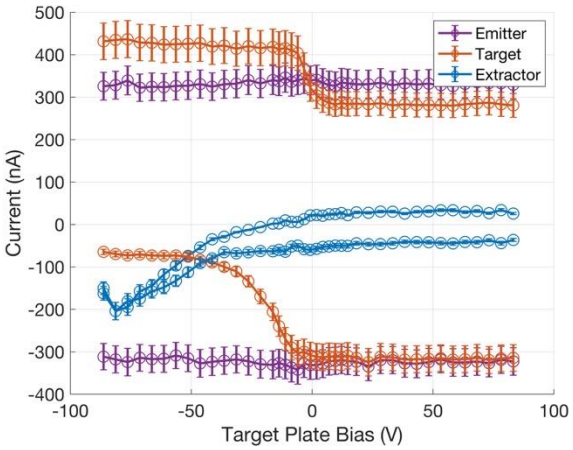

1.8 kV

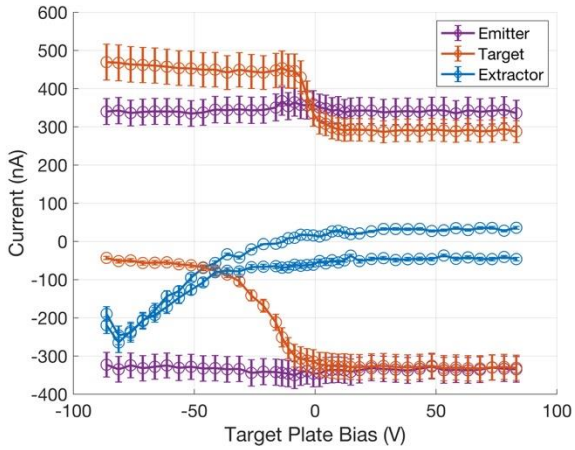

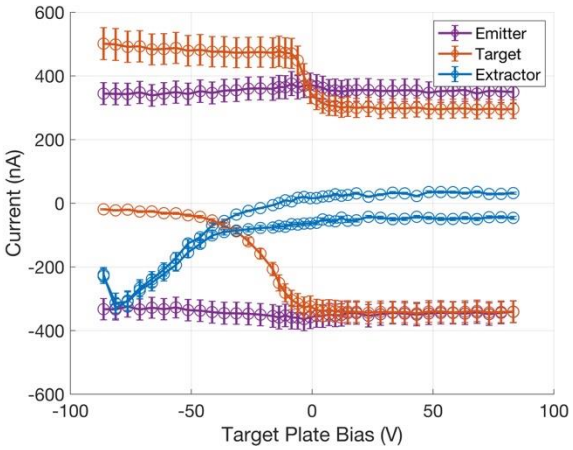

1.9 kV

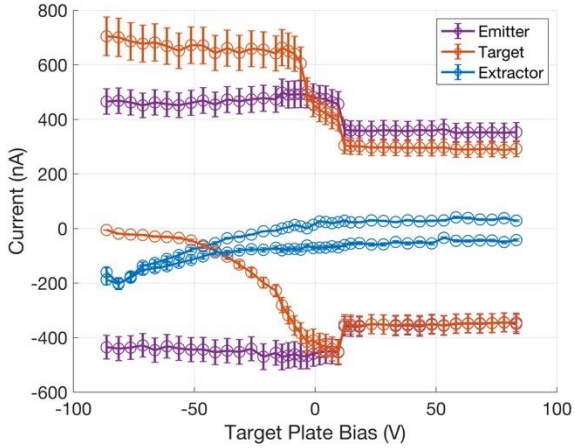

2.0 kV

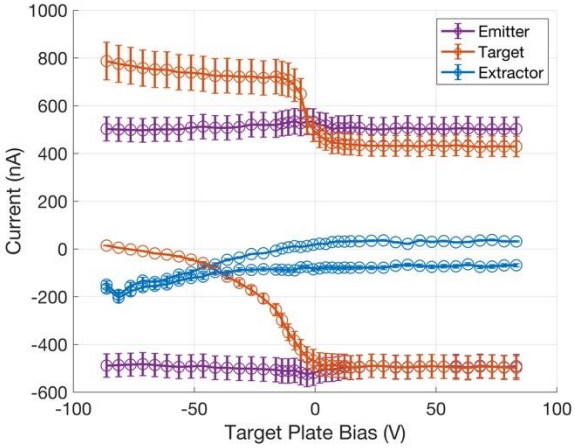

2.1 kV

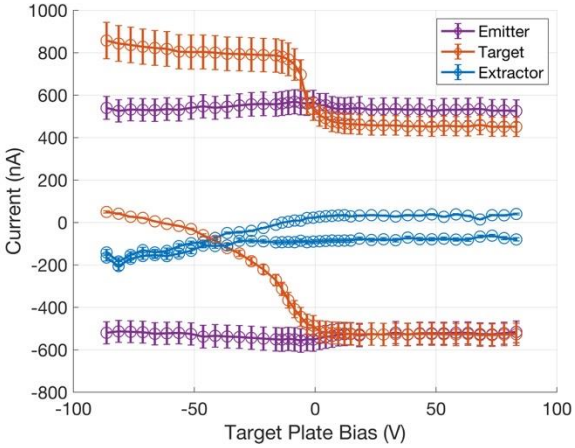

2.2 kV

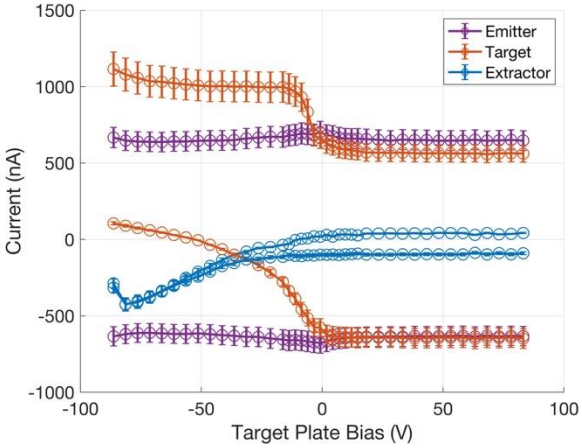

2.3 kV

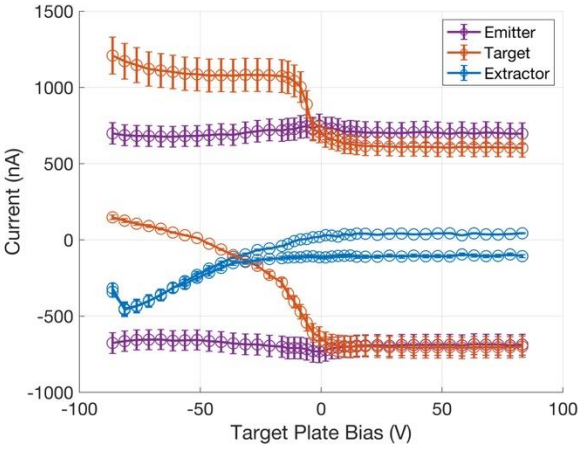

2.4 kV

2.5 kV

Stainless

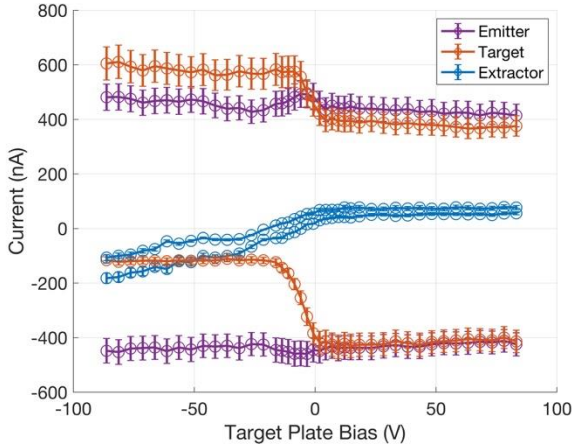

1.8 kV

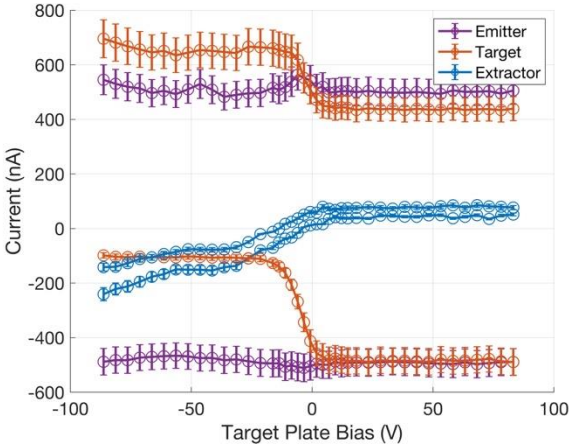

1.9 kV

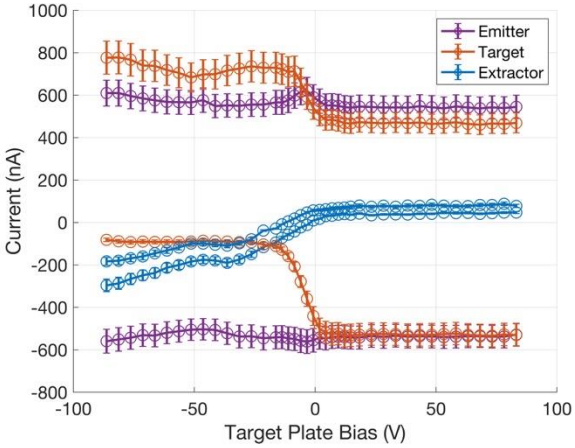

2.0 kV

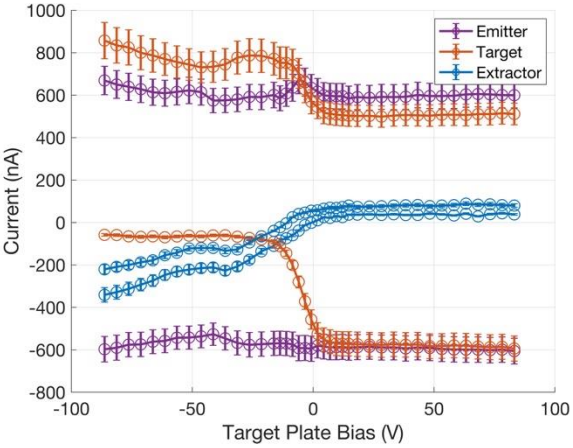

2.1 kV

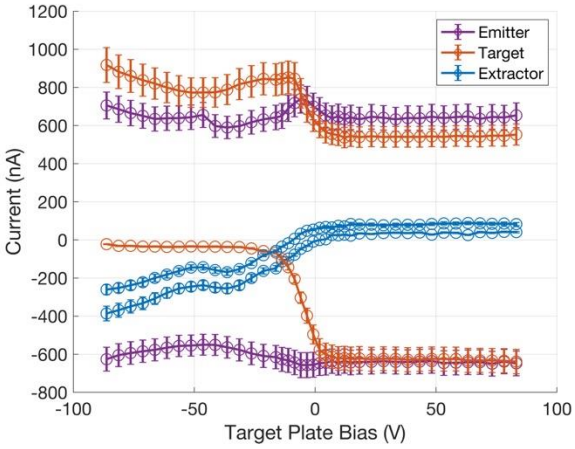

2.2 kV

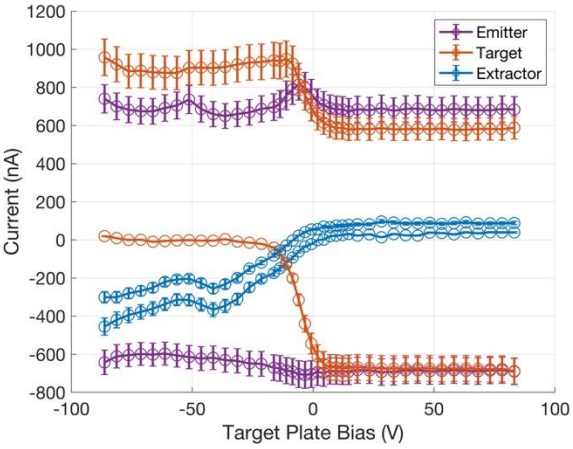

2.3 kV

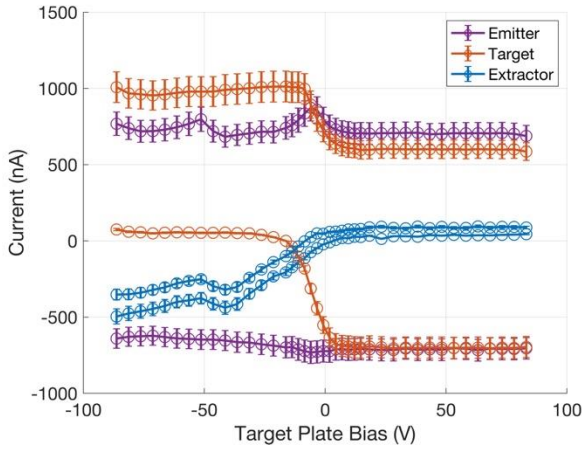

2.4 kV

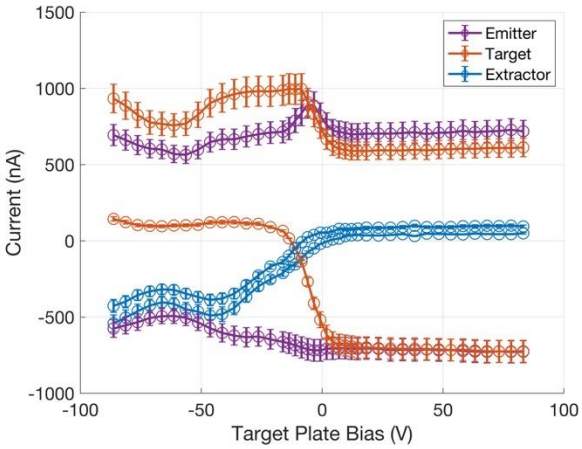

2.5 kV

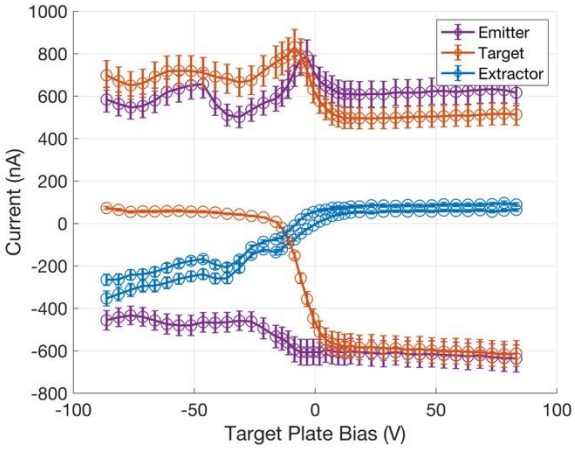

2.6 kV

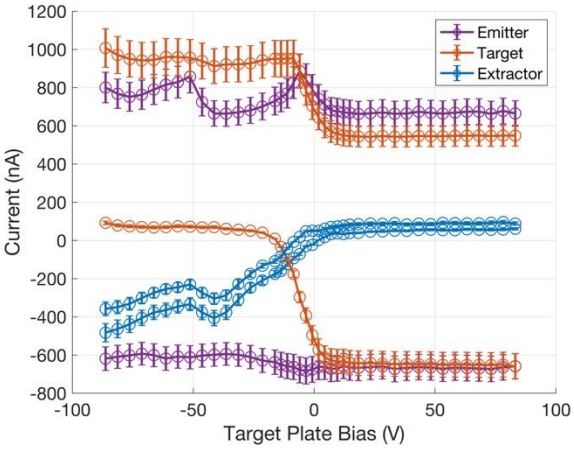

2.7 kV

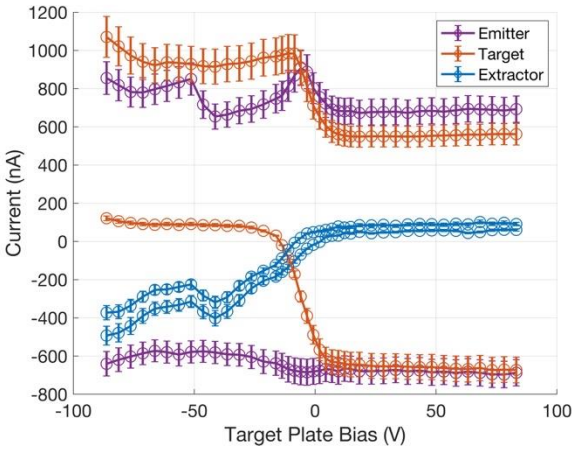

2.8 kV

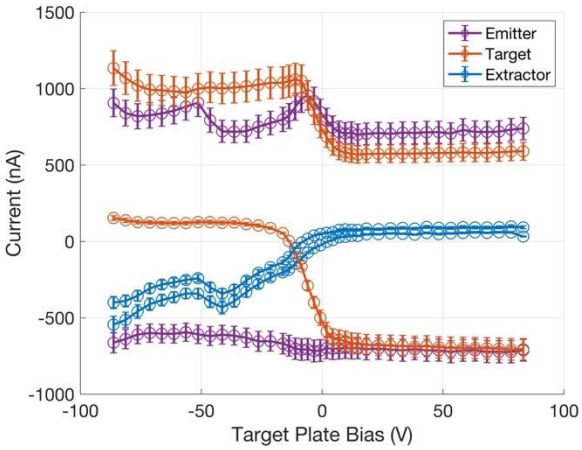

2.9 kV

Carbon Graphite

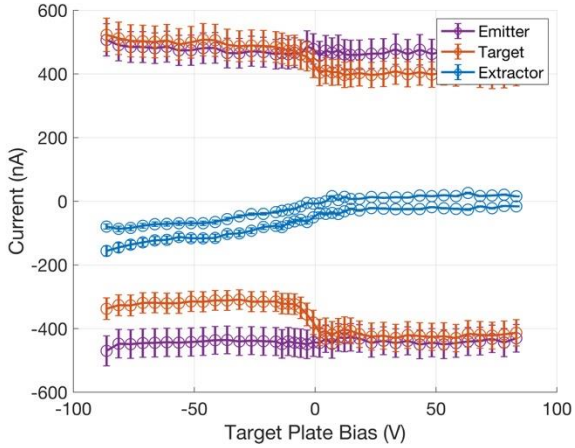

1.5 kV

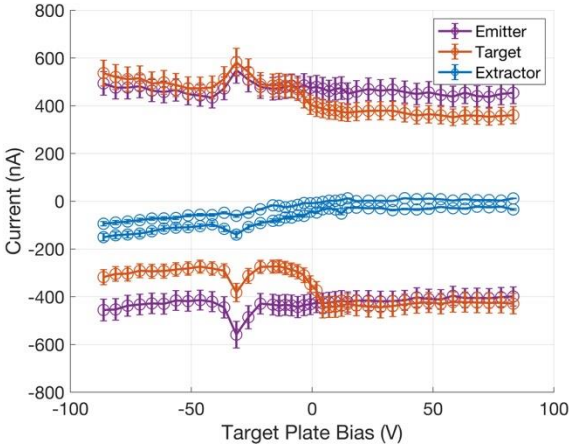

1.6 kV

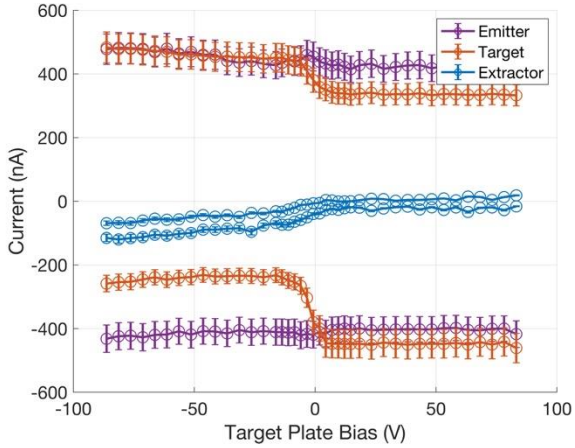

1.7 kV

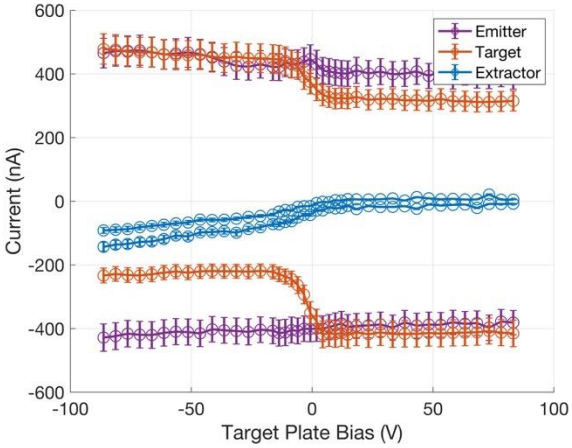

1.8 kV

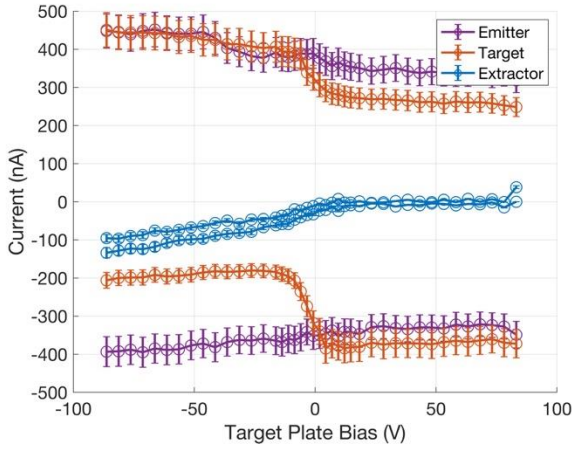

1.9 kV

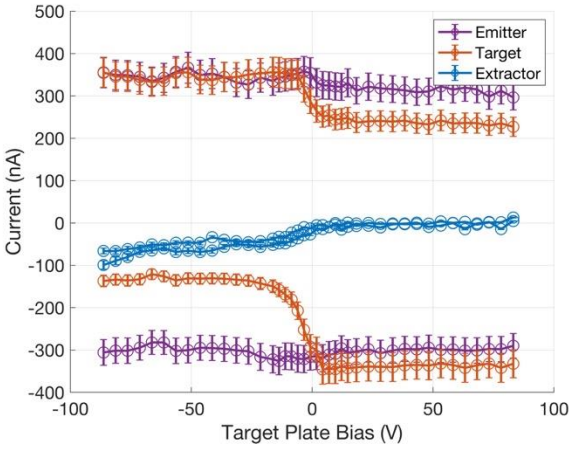

2.0 kV

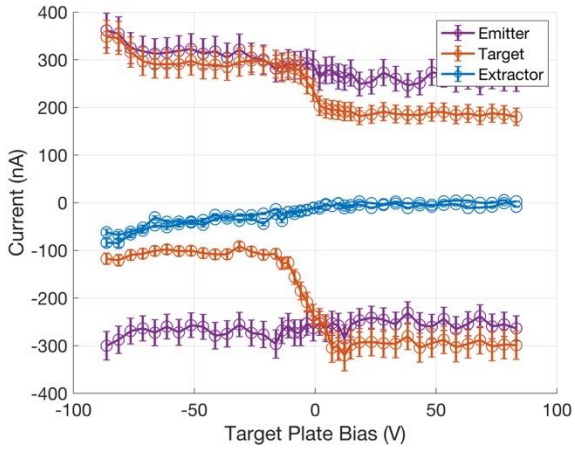

2.1 kV

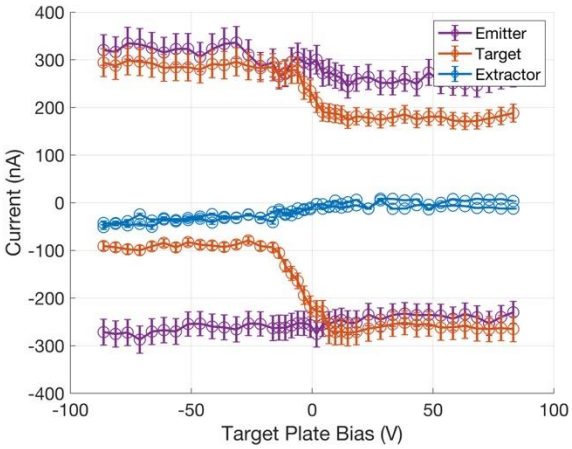

2.2 kV

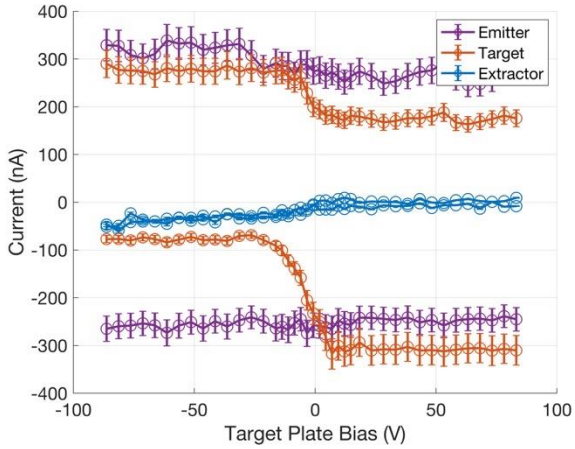

2.3 kV

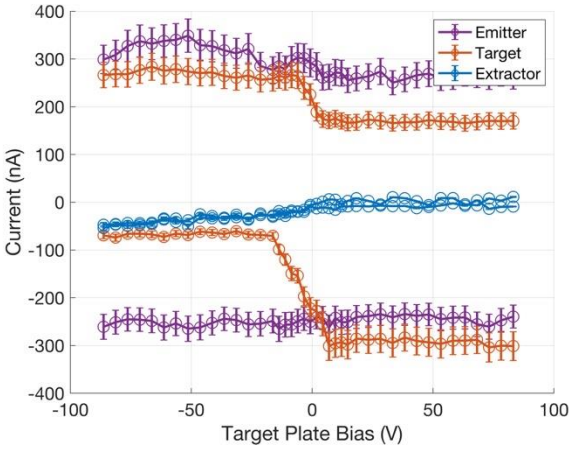

2.4 kV

Titanium

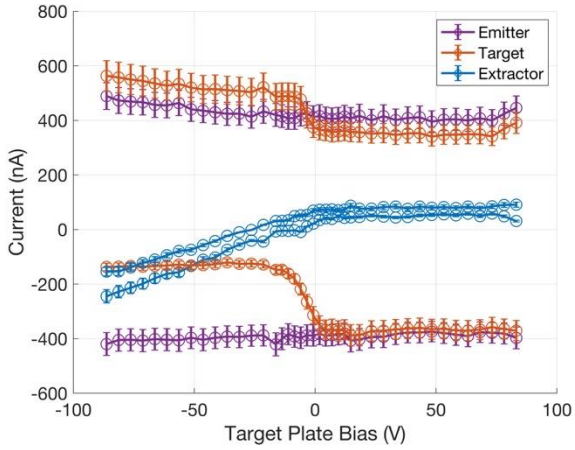

1.6 kV

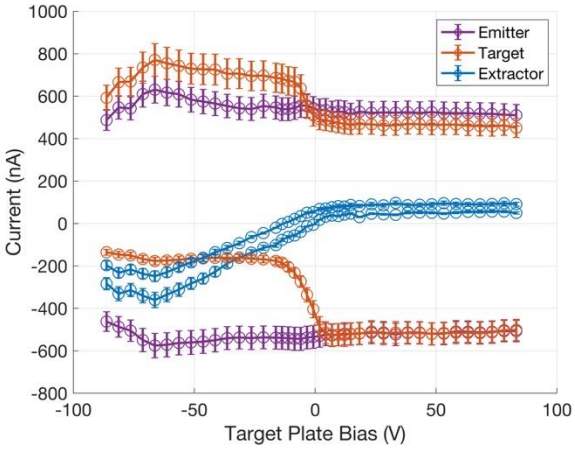

1.7 kV

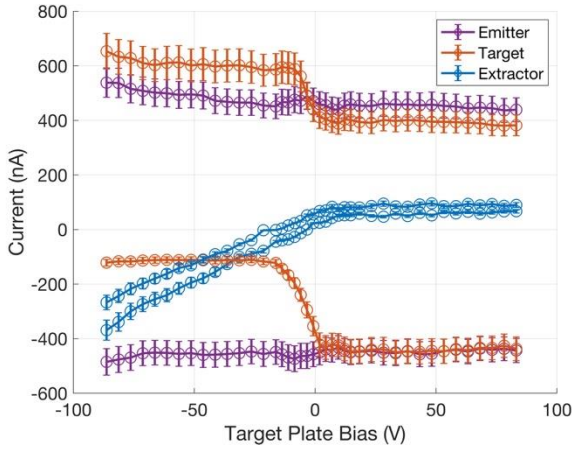

1.8 kV

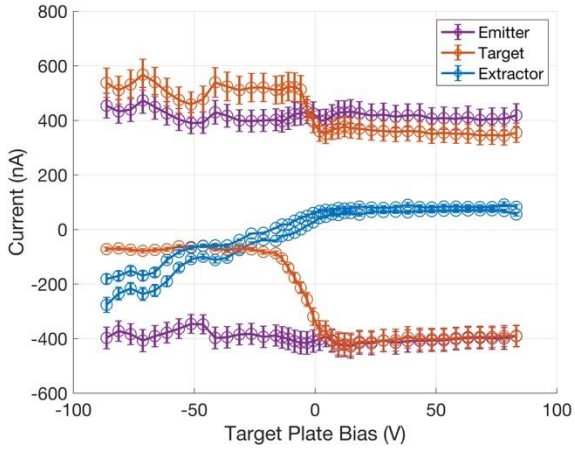

1.9 kV

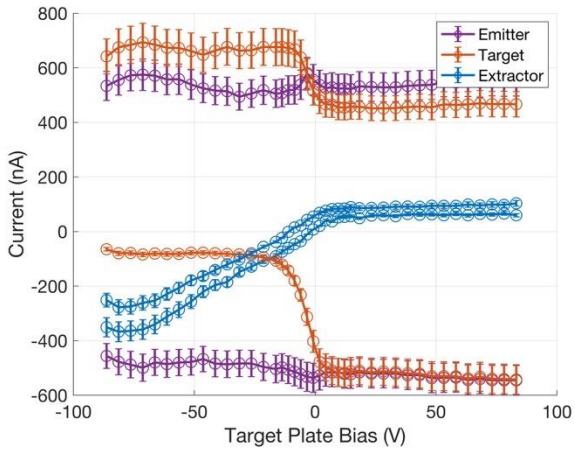

2.0 kV

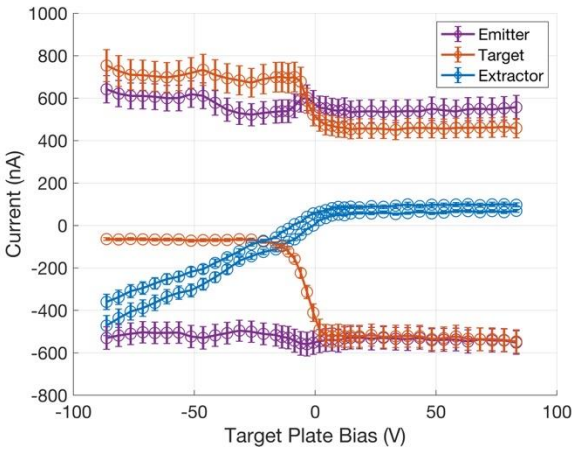

2.1 kV

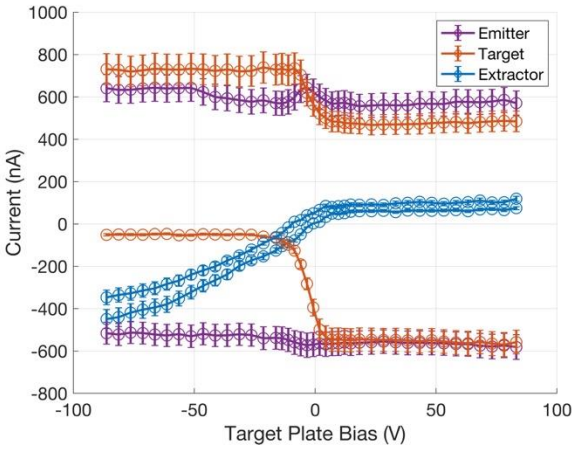

2.2 kV

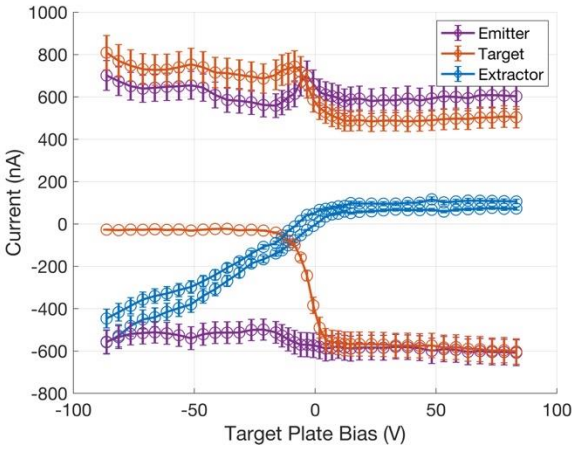

2.3 kV

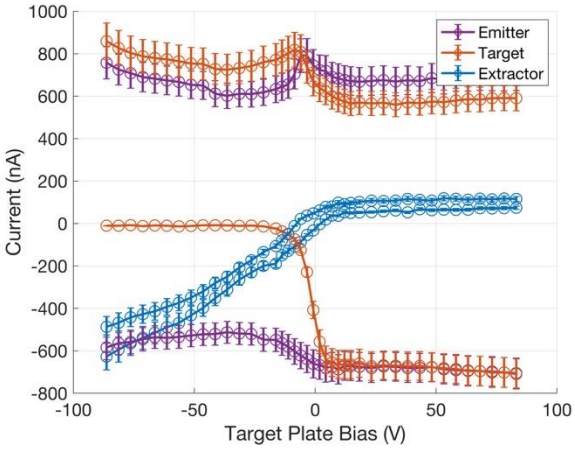

2.4 kV

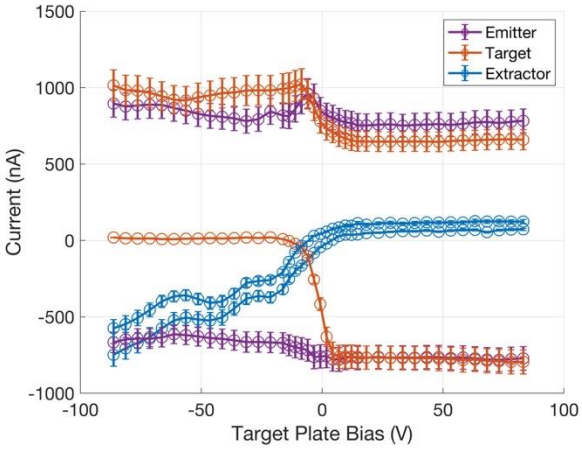

2.5 kV

Nickel

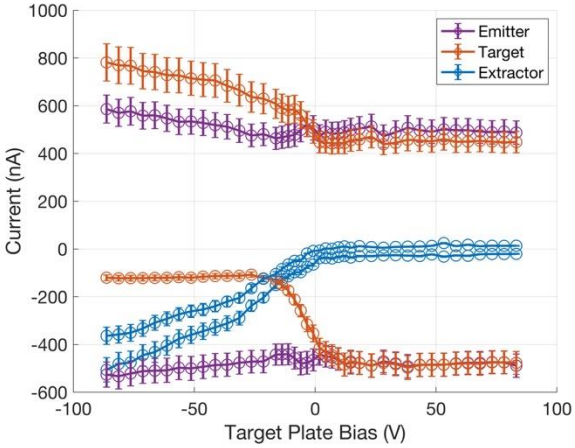

1.6 kV

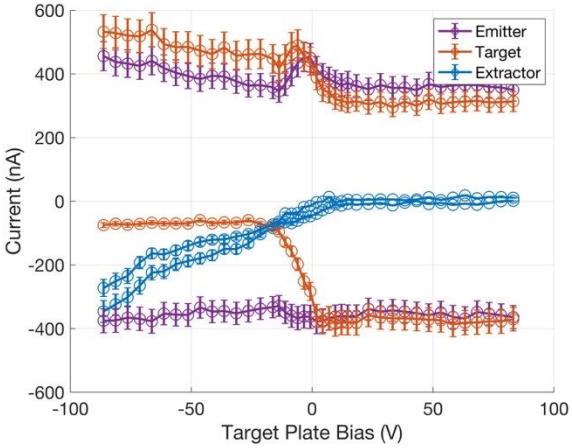

1.9 kV

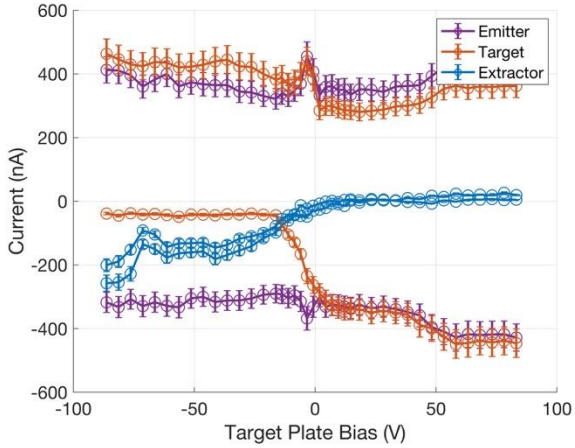

2.0 kV

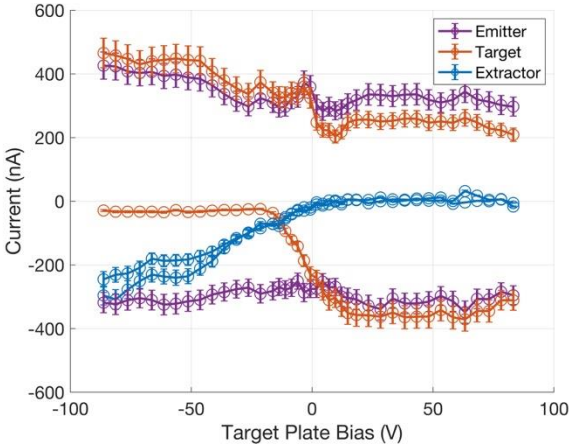

2.1 kV

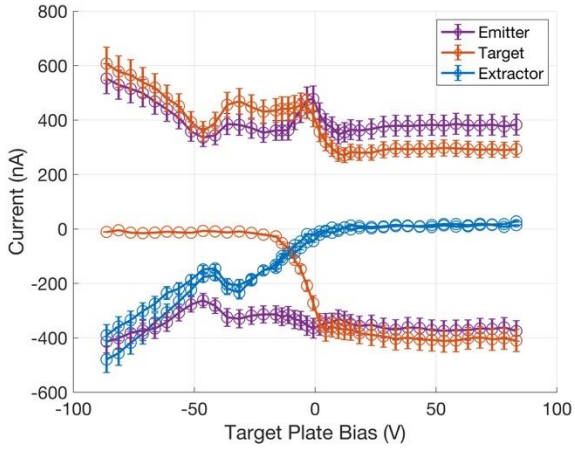

2.2 kV

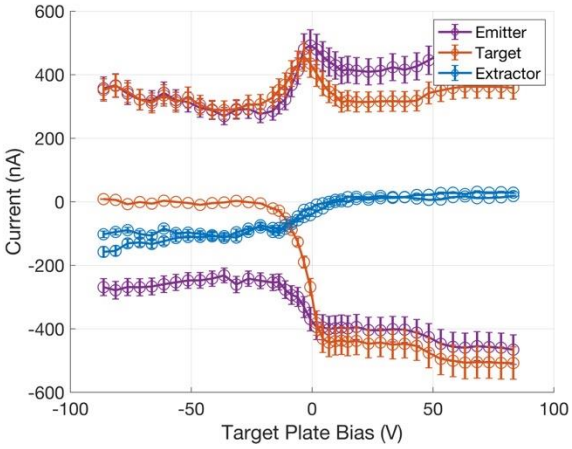

2.3 kV

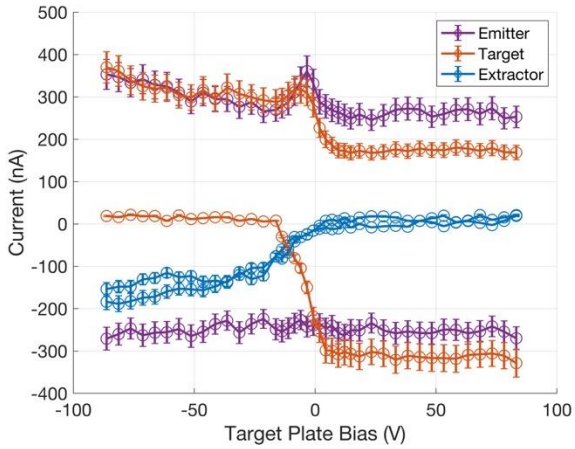

2.4 kV

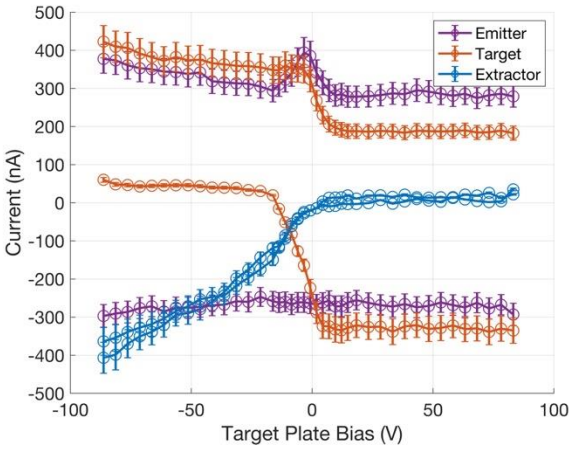

2.5 kV

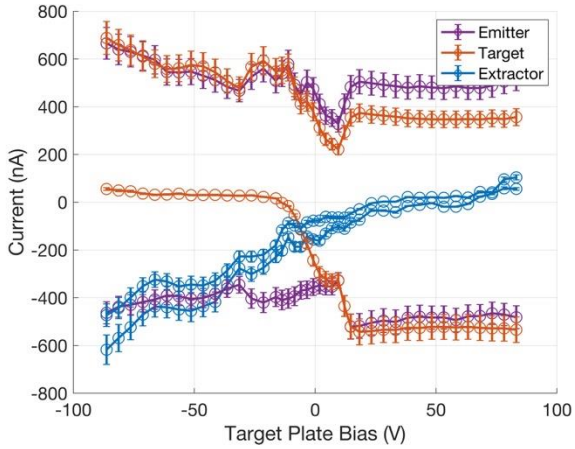

2.6 kV

Tungsten Carbide

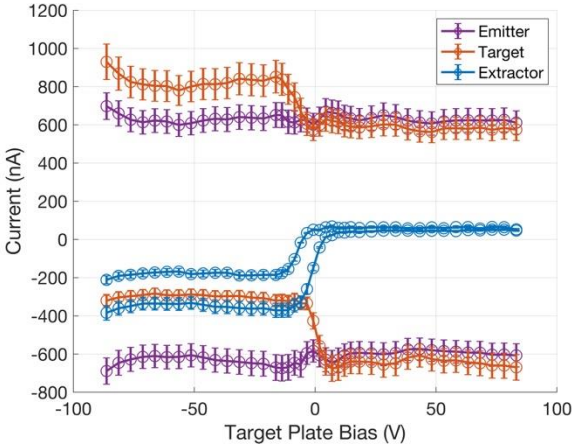

1.7 kV

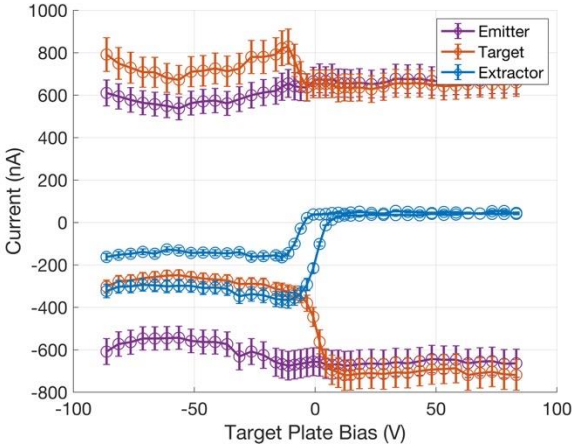

1.8 kV

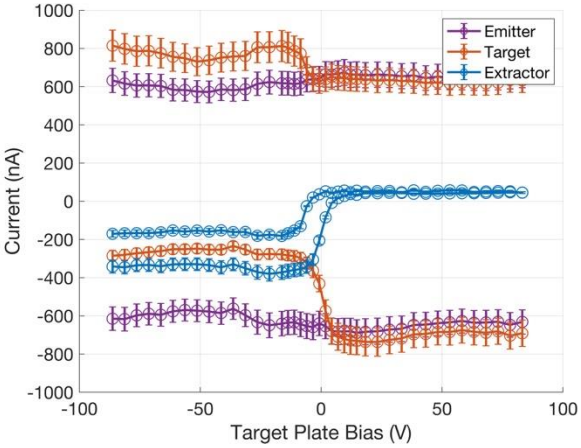

1.9 kV

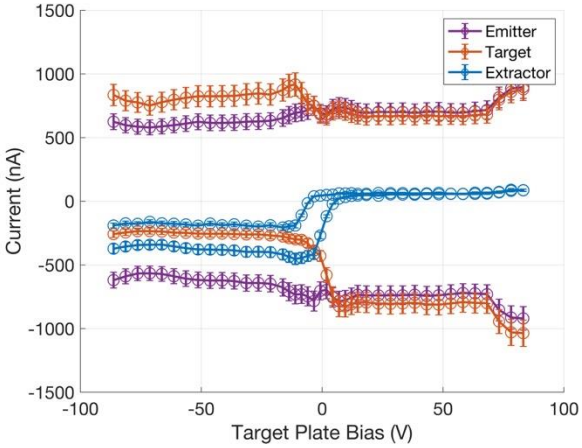

2.0 kV

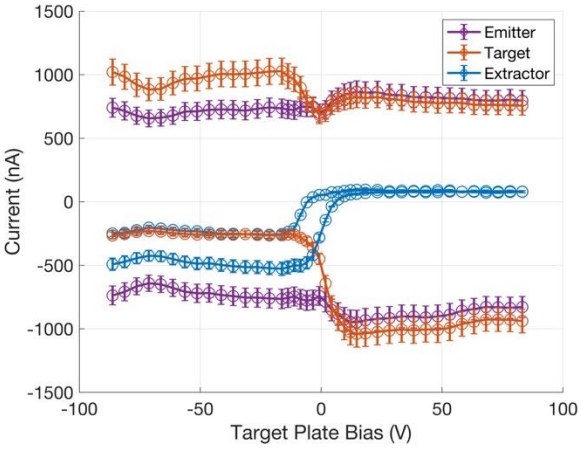

2.1 kV

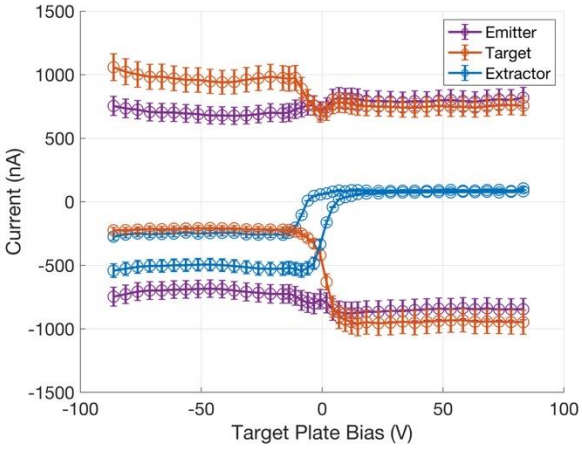

2.2 kV

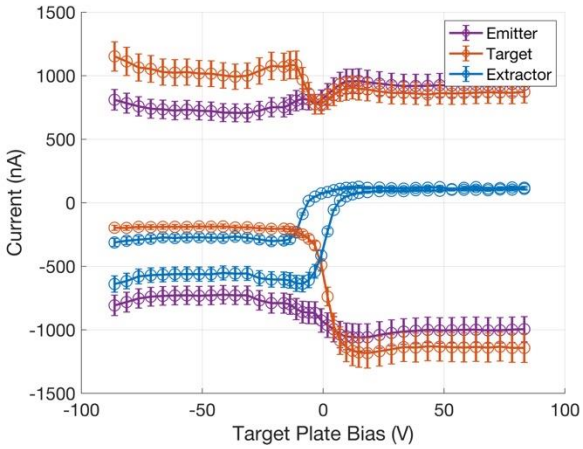
Emitter
Target
Extractor
Current (nA)
Target Plate Bias (V)
1500
1000
500
0
-500
-1000
-1500
-100
-50
0
50
100

2.3 kV

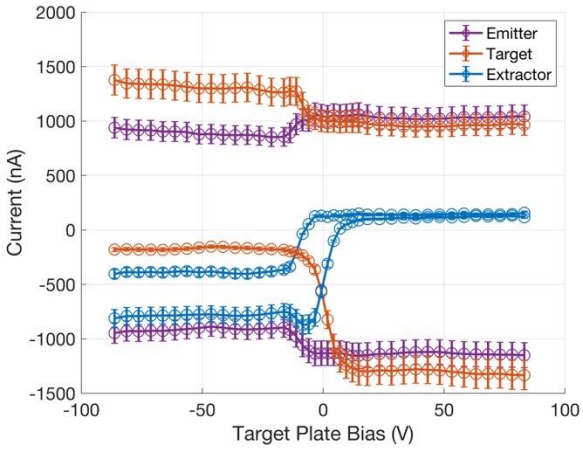
Emitter
Target
Extractor
Current (nA)
Target Plate Bias (V)
2000
1500
1000
500
0
-500
-1000
-1500
-100
-50
0
50
100

2.4 kV

Molybdenum

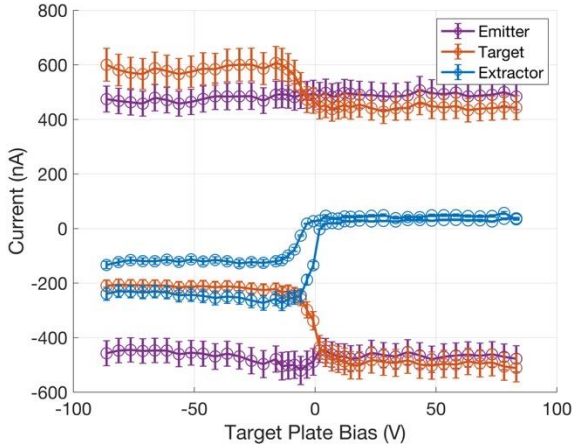

1.7 kV

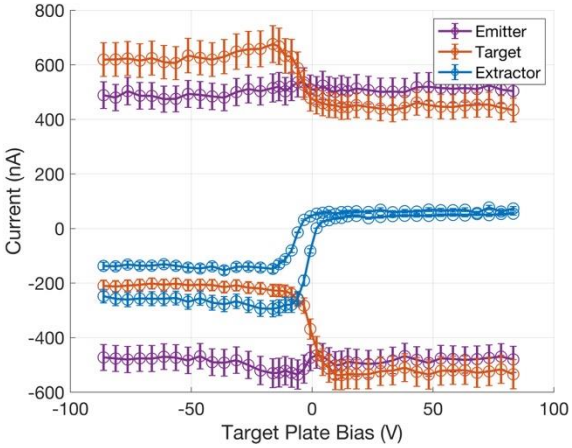

1.8 kV

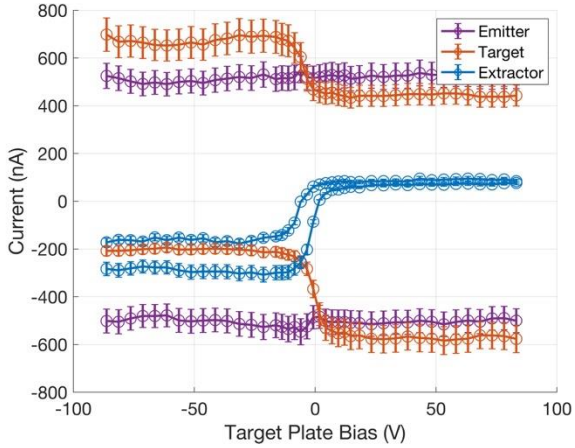

1.9 kV

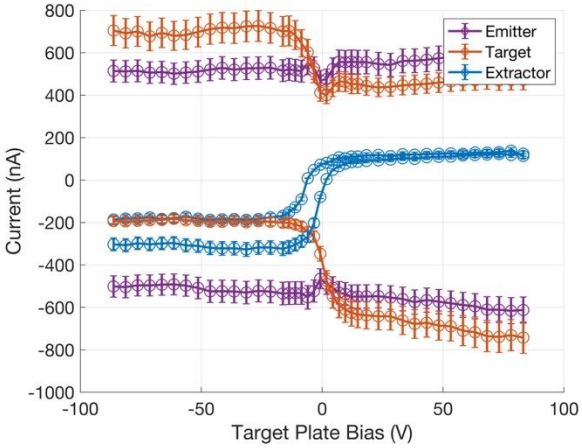

2.0 kV

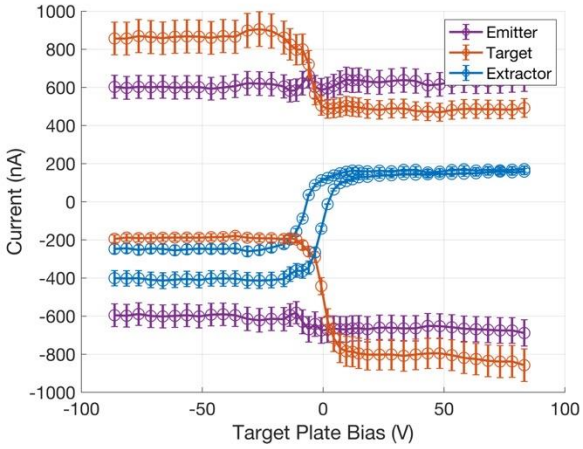

2.1 kV

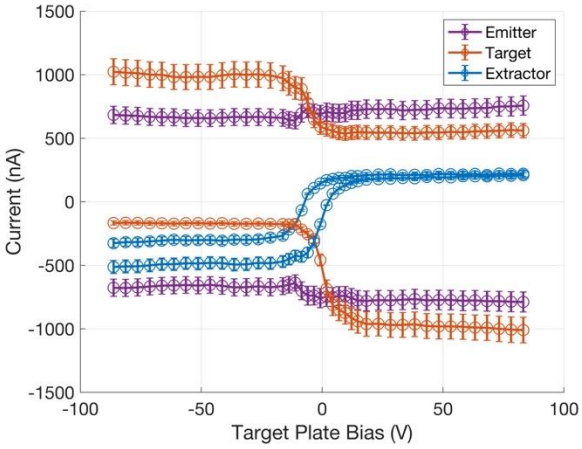

2.2 kV

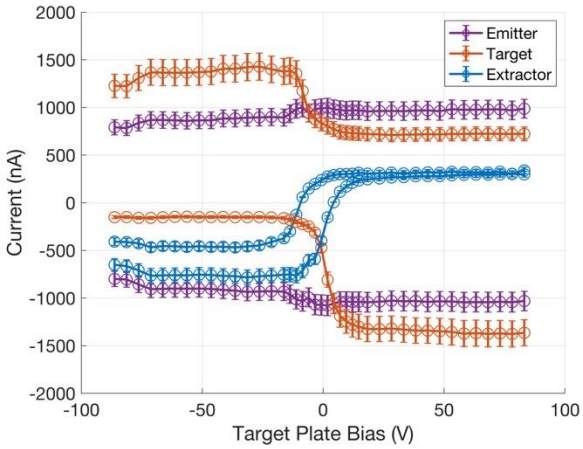
Emitter
Target
Extractor
Current (nA)
Target Plate Bias (V)
2000
1500
1000
500
0
-500
-1000
-1500
-2000
-100
-50
0
50
100

2.3 kV

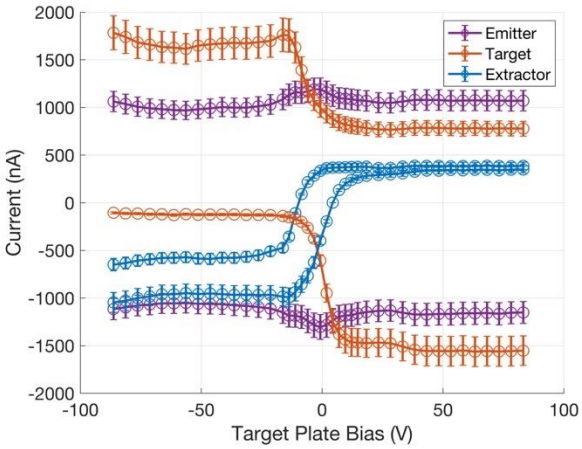
Emitter
Target
Extractor
Current (nA)
Target Plate Bias (V)
2000
1500
1000
500
0
-500
-1000
-1500
-2000
-100
-50
0
50
100

2.4 kV

Gold

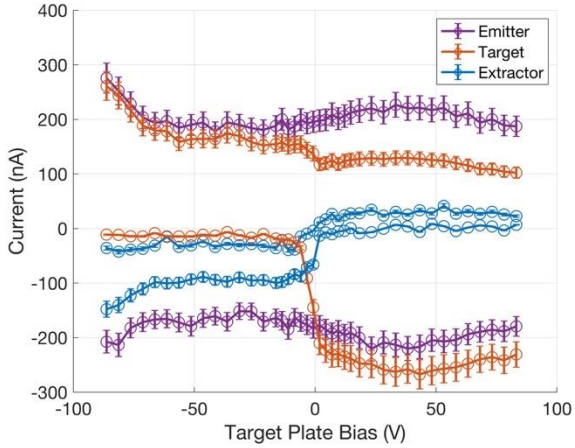

2.1 kV

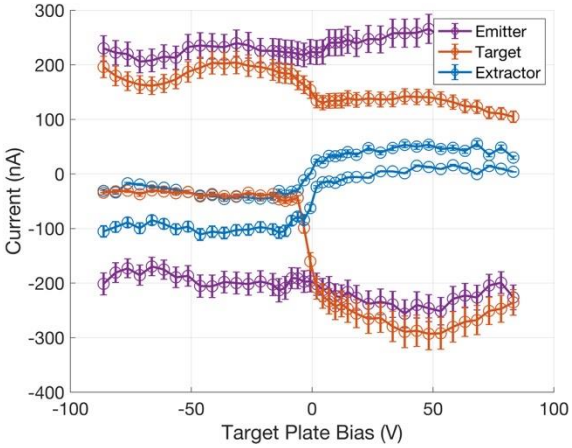

2.2 kV

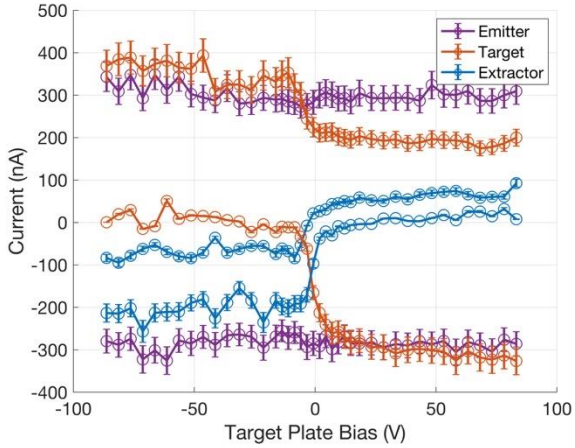

2.3 kV

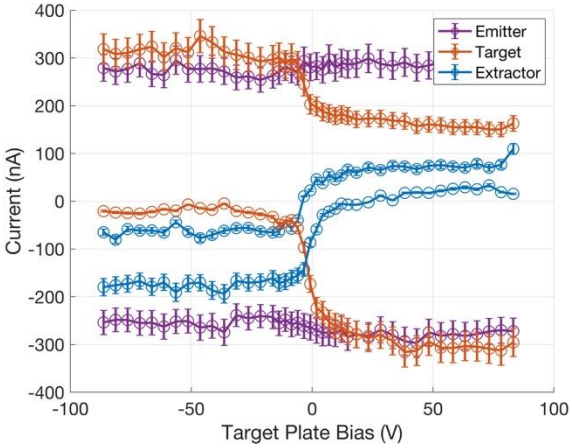

2.4 kV

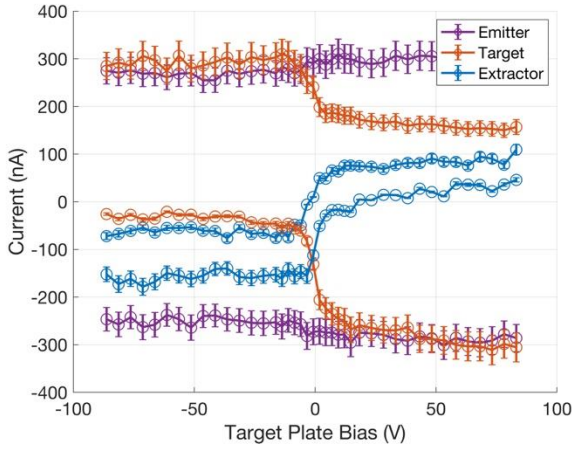

2.5 kV

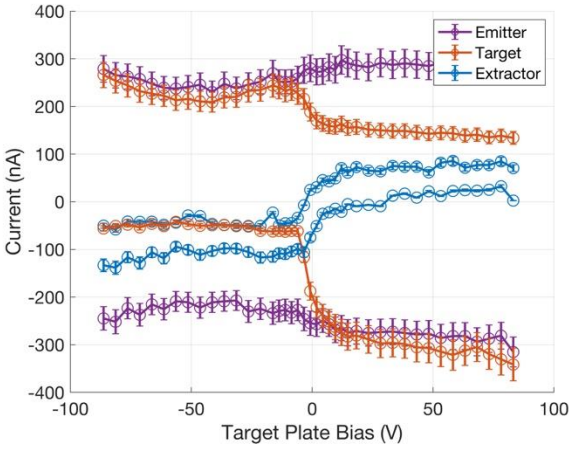

2.6 kV

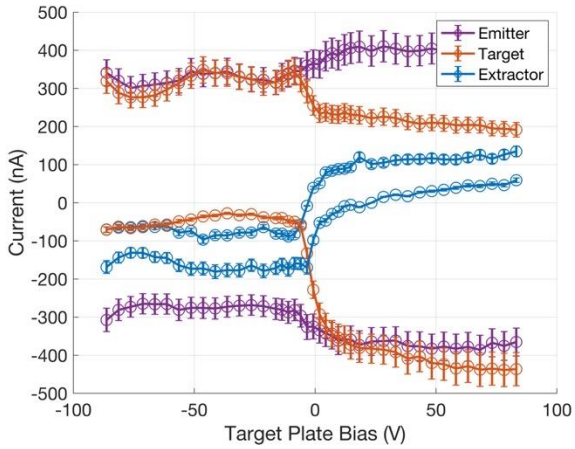
Emitter
Target
Extractor
Current (nA)
Target Plate Bias (V)

2.8 kV

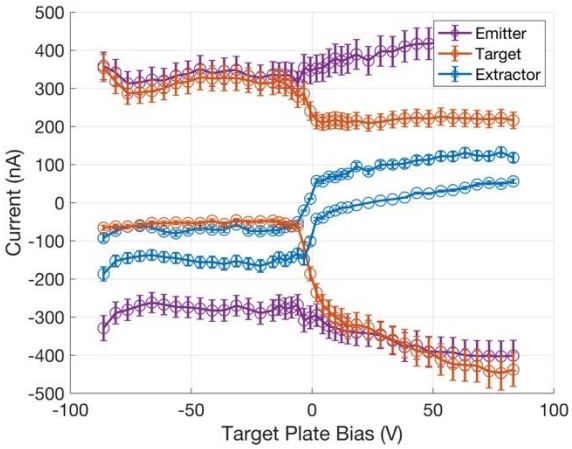
Emitter
Target
Extractor
Current (nA)
Target Plate Bias (V)

2.9 kV

APPENDIX B

EXTERNALLY WETTED TUNGSTEN EMITTER MANUFACTURING PROCEDURE

Supplies:

- > 40 mm long sections of straight 0.5 mm diameter tungsten wire (1 section for each emitter)
- ~ 5 mm long straight sections of 0.25 mm diameter tungsten wire
- Magnetic stirrer/hot plate with temperature probe
- 2 100 mL beakers
- Solid NaOH
- Solid $K_3Fe(CN)_6$
- Distilled Water
- Wire clip attached to long, non-conductive rod
- 50 V, 3 A power supply
- Optical Microscope
- Magnifying glass/lens
- Additional wire lead for NaOH solution
- Nitrile Gloves
- Safety Glasses
- Fume Hood
- Two Waste Disposal Containers

Safety Information:

Do not attempt etching outside of a chemical fume hood facility

NaOH MSDS: https://fscimage.fishersci.com/msds/21300.htm

$K_3Fe(CN)_6$ MSDS:https://beta-static.fishersci.com/content/dam/fishersci/en_US/documents/programs/education/regulatory-documents/sds/chemicals/chemicals-p/S25489.pdf

Step 1: Electrochemical Etching

1. Put on safety glasses and nitrile gloves
2. Use a digital scale to measure out 2 g NaOH in a 100 mL beaker
3. In another 100 mL beaker, measure out 50 mL of distilled water and pour into the first beaker
4. Use the magnetic stirrer to stir the mixture until all of the NaOH has dissolved
5. Insert a wire lead securely into the NaOH mixture and attach the negative terminal of the power supply
6. Take a section of 0.5 mm diameter tungsten wire and clip one end into the wire clip such that you can lower the other end of the wire into the mixture. Attach the positive power supply lead to the wire clip.
7. Set the power supply to full current at 50 V and slowly lower the very end of the tungsten wire section into the solution. When it makes contact, there will be a significant fizzing around the wire due to the electrochemical etching. Do not submerge the wire past the point where fizzing begins.
8. Carefully dip only the very tip into the solution for periods of no longer than 2 seconds. Observe the tip by eye or by magnifying glass so check the progress of the etching. If the tip is getting too sharp very short dips (pull the tip out of the solution as soon as the fizzing

begins) may assist in getting a rounder tip shape. After the tip has formed, use quick dips (no more than 0.5 seconds) in the solution to get the desired tip shape.

9. When the tip appears acceptable by eye or magnifying glass observation, use the optical microscope to get a closer look. The wire should have a smooth, concave curvature down the entire tip. The tip should be rounded, but not sharp. The figures below show an image of a working emitter at UIUC.
10. Continue short dips in the solution, changing the voltage as necessary until the desired tip shape is achieved.
11. Finally, turn the power supply to 5 V and insert the entire needle into the solution for a few seconds. This removes the oxide layer making it easier to spot weld in the next step. Then, spray the needle down with distilled water and repeat for other emitters.
12. Use the power supply at 5 V to remove the oxide layer of all 0.25 mm diameter wire sections as well. Spray down with distilled water.
13. Pour the NaOH solution into a safe, labeled chemical waste container

Step 2: Spot Welding the Ionic Liquid Reservoir

1. Ultrasonically clean all needles and 0.25 mm wire sections in water, then acetone or ethanol. Dry in rough vacuum or with dry air.
2. Contact Ernest Northern at the MRL machine shop and bring the wire sections to be spot welded. He should have the spot welder mount for this project. Bring extra sections of 0.25 mm wire in case some are dropped and cannot be found.
3. Insert the 0.25 mm wire section into the lower groove of the mount and the needle in the top groove perpendicular to the smaller wire with the tip distanced 3 mm from the smaller wire.

Take care not to bump the emitter tip as it can be easily damaged!

4. Set the spot welder to 700 Volts and press down on the wires
5. If the wires do not join, attempt the weld again and try to weld in the same spot to avoid further spots of damage on the emitter
6. Repeat until each emitter is welded together

Step 3: Microetching of the tip-crossbar assembly

1. Put on nitrile gloves and safety glasses
2. Use a digital scale to measure 8 g of NaOH in a 100 mL beaker
3. Measure out 100 mL of distilled water in another beaker and pour into the first beaker
4. Use the magnetic stirrer to stir the mixture until all of the NaOH has dissolved
5. Pour half (~50 mL) of the solution into the second beaker
6. Put the first beaker of solution on the hot plate and set to 90 C with the temperature probe inserted into the mixture. Do not let the solution exceed 100 C.

7. When the solution reaches 90 C, begin adding $K_3Fe(CN)_6$ in small amounts and using the magnetic stirrer until it has all dissolved. Continue this process until you can stop the magnetic stirrer and see a thin crust form on top of the reddish-brown solution or no more $K_3Fe(CN)_6$ will dissolve

The solution will stain surfaces – take care not to spill

8. For the rest of the process, if $K_3Fe(CN)_6$ begins to solidify on the surface, add a bit of the second beaker of NaOH solution to bring it back to saturation
9. With the solution saturated with $K_3Fe(CN)_6$ and maintained at 90 C dip the emitter tip-crossbar assembly into the solution for ~ 45 seconds
10. Rinse the emitter with distilled water and dry with dry air
11. Pour the microetching solution into a safe, labeled chemical waste container

The emitter manufacturing is now complete. Store emitters in a secure place where they can avoid bumps or falls.

Emitter Preparation and Loading:

1. Rinse emitter with water and carefully wipe with a wet kimtech wipe to remove large dust and strands
2. Ultrasonic clean emitter in a beaker of distilled water for 10 minutes to remove smaller particles
3. Ultrasonic clean emitter in a beaker of IPA, ethanol, or acetone for 10 minutes to remove the water and “dry” the emitter

4. Dry the emitter by gently blowing dry air or nitrogen or by pumping down to rough vacuum in the desiccator for a few minutes
5. Use a magnifying glass or eyepiece to check that no large debris is remaining on the emitter. If the emitter does not look clean, restart the cleaning process.
6. Place the emitter in the copper mount and use the heat gun to heat up the tip/crossbar for 1 minute (spend 15 seconds from each side of the emitter). This helps the liquid adhere to the surface.
7. Use a 0.05 mL syringe loaded with ionic liquid to make a drop on the end of the syringe needle. Drag the drop of IL over the emitter tip and back to the crossbar. Run it over each side of the emitter and the tip several times to ensure full coverage. Deposit the remaining IL on the crossbar assembly. There should be enough IL to form a drop around the entire wire, but not much more than that. Very large reservoirs are more prone to being pulled to the extractor.
8. Insert the copper emitter mount into the extractor mount and tighten the set screws on the copper mount with the emitter tip close to centered on the extractor hole and the tip in-plane with the extractor face.
9. Use the nuts on the inner plate of the extractor mount to move the extractor back and forth, and to angle it such that the emitter tip is perfectly centered on the extractor hole. This can be checked using a magnifying glass or eyepiece looking straight down the other side of the extractor hole. You should be able to see the pinpoint of the emitter tip perfectly in the center of the circle.
10. Once the emitter is centered on the extractor hole, check again that it is still in place with the extractor face. A small gap (< 0.2 mm) will probably be okay.

11. Wrap kapton tape or other shielding around the emitter/extractor assembly such that any surfaces electrically connected to the emitter are fully covered.
12. The emitter is ready to be loaded into the vacuum chamber.

APPENDIX C

POST-TEST ANALYSIS OF SURFACES

Post-test images of several surfaces were taken using the Keyence VK-X1000 laser microscope. After exposure to the electrospray plume, some surfaces exhibited visible signs of surface modification. Further analysis is needed to determine the cause of this modification, but there are several possibilities including sputtering, chemical reactions between the [Emim][BF_4] ions and surface atoms, or a condensed ionic liquid layer. The images below on the left show nickel, tungsten carbide, and molybdenum surfaces placed 1 cm from the extractor with varying levels of surface modification. The images on the right show the height map of the surface at the same length scale. Only the nickel height map reflects the visible changes in the surface from the optical images.

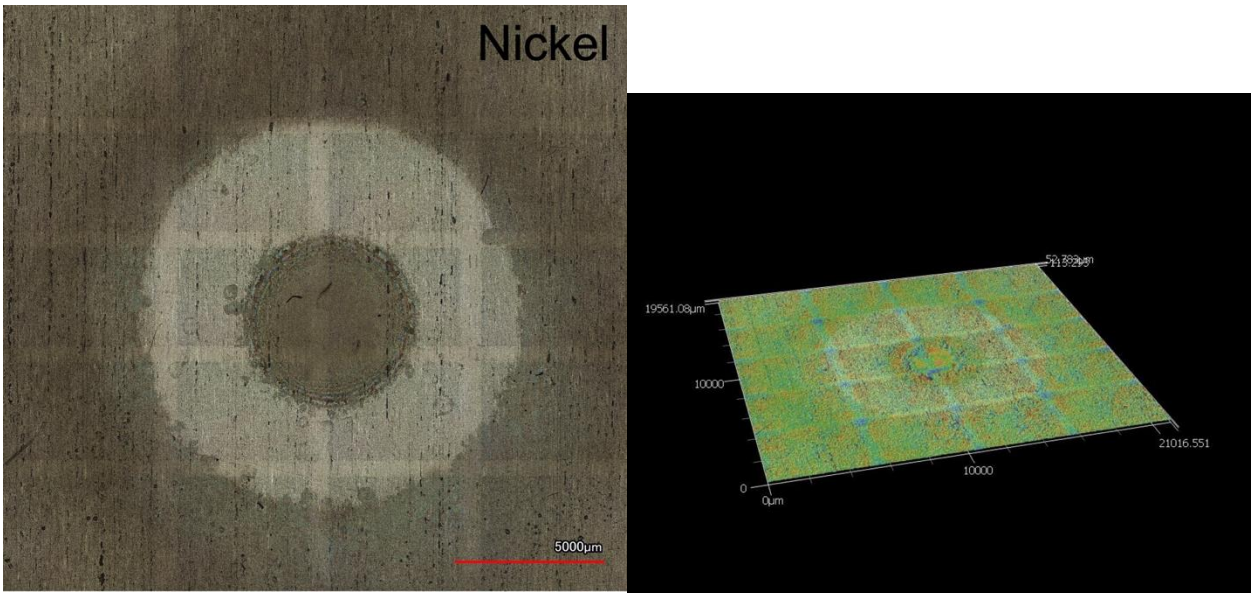

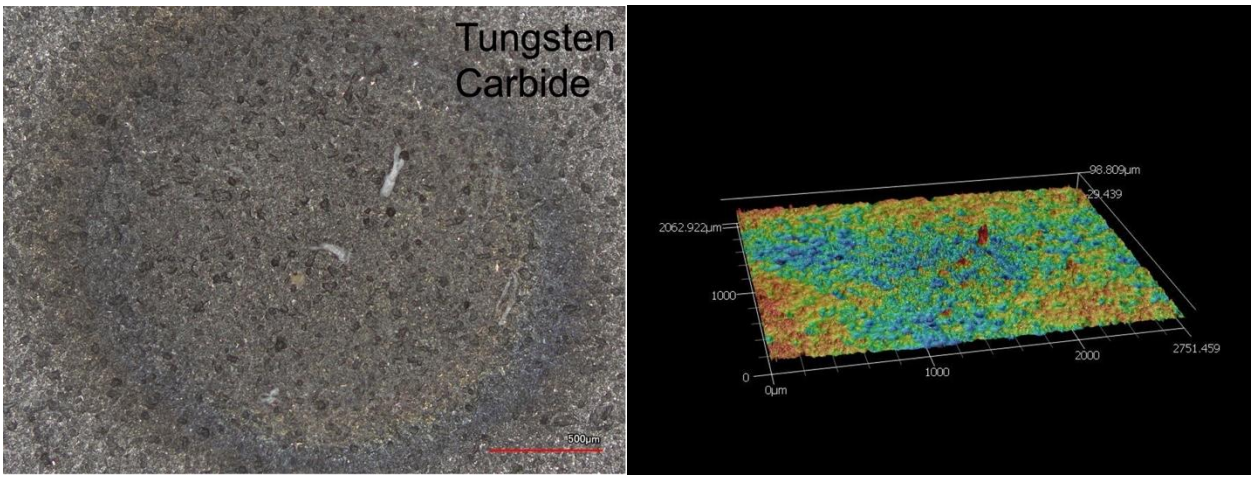

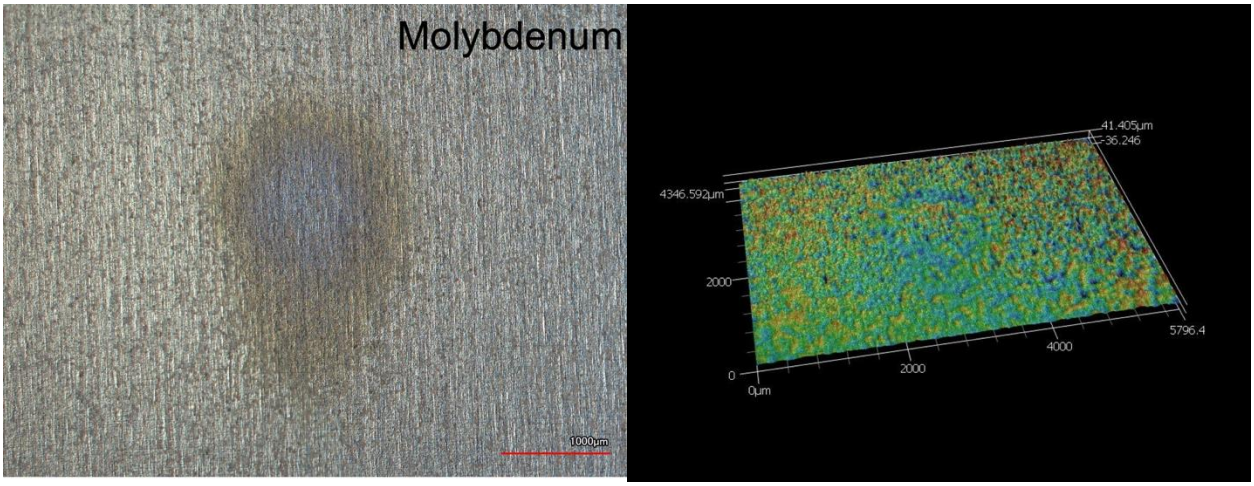

A post-test stainless steel extractor grid and aluminum collector plate were received from The University of Southampton after tests were performed using their porous glass electrospray thruster. The image below on the right is of a piece of the extractor which was not exposed to the electrospray plume. The image on the left is of a piece in the center on the upstream side of the extractor. The surface roughness increases from 2.43 μm to 10.25 μm after the thruster is tested and there is very clear discoloration and change in surface structure.

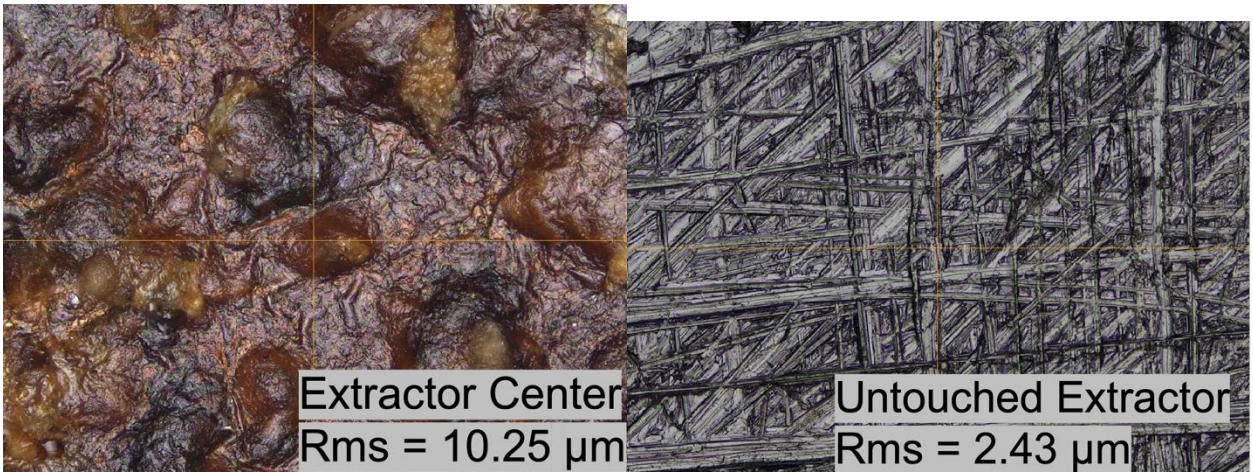

The image below shows a scan from the center (left) to the outside (right) of the extractor grid, as the intensity of exposure to the electrospray plume goes from greater to lesser. The top figure shows the optical image and the bottom figure shows a horizontal linear height map across the center of the image.

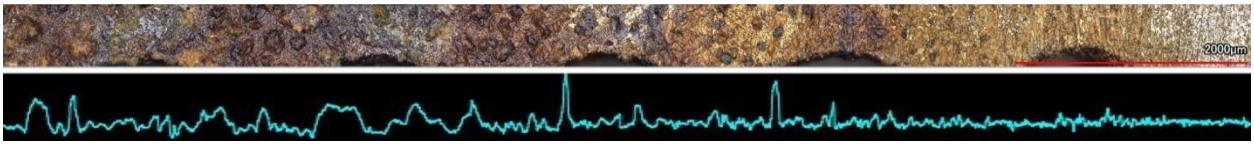

The aluminum collector plate has been imaged and is shown below. The top image is a part of the plate that was not exposed to the electrospray plume. The bottom image is a scan of a large section of the plate that has been exposed to the plume. While the large scratch marks on the surface were likely there before testing, the craters found all over the surface appear to be a sputtering phenomenon where, instead of every ion removing a certain number of surface atoms, the surface is damaged in certain places to a point where larger chunks of surface material are removed by further impingement. It is also possible that once a crater is formed, it becomes easier for further sputtering to occur.

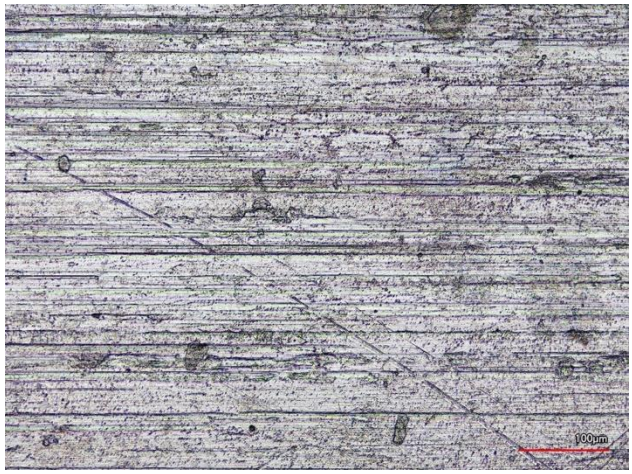
100µm

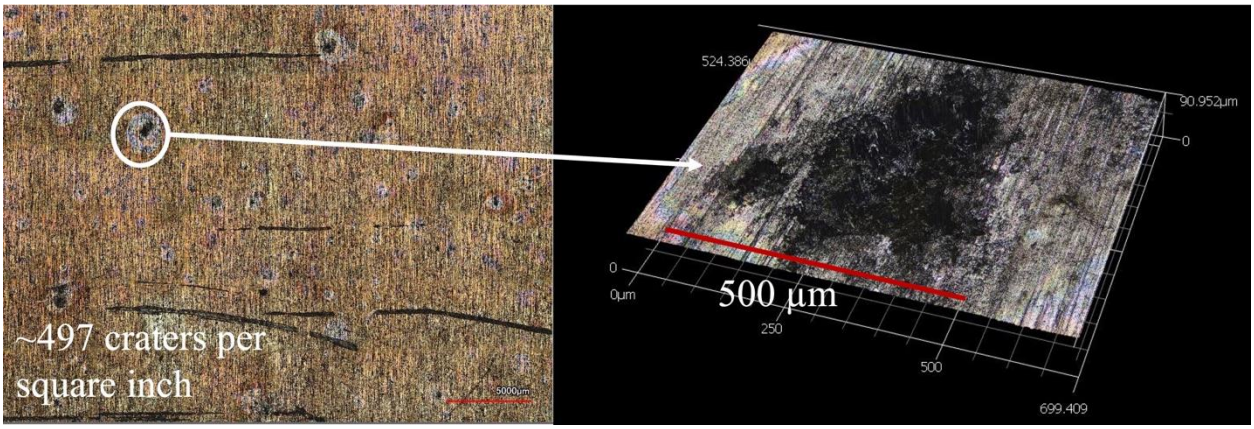
~497 craters per square inch
5000µm
524.386
90.952µm
0
0
0µm
500 µm
250
500
699.409

APPENDIX D

NANONEWTON RESOLUTION THRUST STAND

Introduction

An impingement plate style thrust stand consists of an impingement plate with intercepts the plume of a thruster and collects all the momentum from the exhaust, and a force probe pressed against the back side of the impingement plate to measure the total force applied to the plate by the thruster. In the < 100 μN regime, impingement plate thrust stands typically quickly lose effectiveness due to insufficient reoslution of force probes and very high noise-to-signal ratios (up to 1000-1). Chakraborty et. al. have designed an impingement plate style thrust stand with a maximum thrust level of 100 μN and a thrust resolution of 10 nN [27,28]. This thrust stand is being reconstructed at the University of Illinois Urbana Champaign Electric Propulsion Laboratory. A brief description of the operation of the thrust stand is given here but more details are given in Refs. [27,28]. The main purpose of the description here is to provide a summary of the previous work on this project at UIUC and a guide to its continuation.

Impingement Plate

The structure of the impingement plate and how it is mounted affects how the plume momentum is absorbed and transferred to the force probe. The equation below gives the thrust resolution of the thrust stand.

$$F_{res} = (1 + \frac{k_p}{k_f})F_{\Delta}$$

where k_p is the spring constant of the impingement plate, k_f is the spring constant of the force probe (50 N/m), and F_{Δ} is the force resolution of the force probe (5 nN). To achieve below 10 nN thrust resolution, the spring constant of the impingement plate must be $\leq$ 50 N/m. The natural

frequency of the plate is designed to be between 50-100 Hz to avoid resonance with the pulse frequency of the thruster (described later – a few Hz), facility vibration (< 1 Hz), or vacuum pump vibration (100's Hz). The frame of the impingement plate at UIUC was manufactured using the same dimensions as given in Ref. [27] and is shown in the figure below.

The frame is manufactured from one rectangular section of 0.13 mm thick aluminum sheeting. The sheet is placed inside a two-piece press with 0.65 mm ridges and indents to form the H-shaped ridges in the structure. The UIUC School of Chemical Sciences machine shop laser cutter is used to cut out the frame as seen above. The laser cutter will need to be located by the ridges and will require 20-30 passes to adequately cut through the aluminum sheeting. The frame will then need to be carefully pushed out from the cut sheet. This process should be done slowly and gently as it is easy to bend and break the four arms that hold the H-shaped frame structure. Once the frame has been formed, a sheet of ARClear 8154 adhesive should be attached to the front followed by a

sheet of aluminized mylar. If the impingement plate will be impinged upon by charged particles, a small hole should be created in the mylar sheet and adhesive and filled with EPOTEK H20S conductive epoxy such that the aluminum layer on the front of the plate is electrically grounded to the structure. The figure below shows the completed impingement plate mounted to the thrust stand structure.

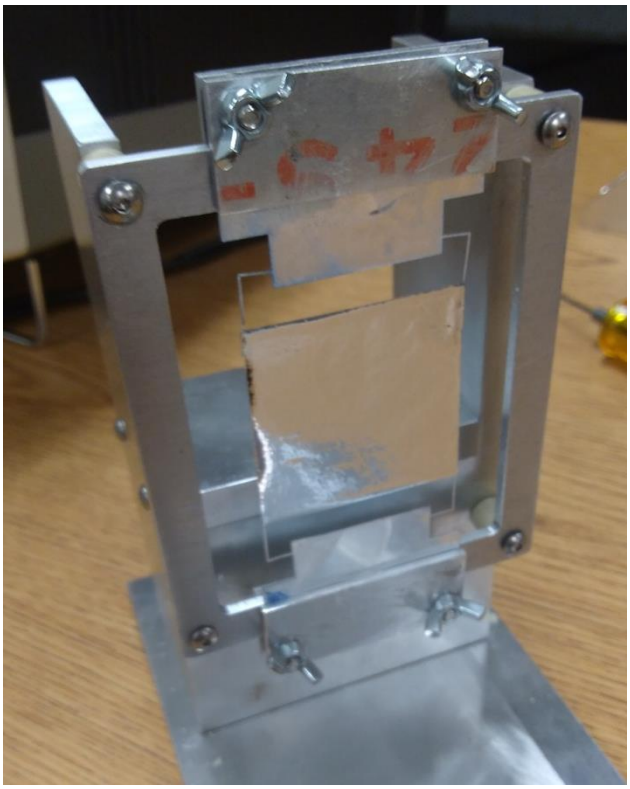

The spring constant of the completed impingement plate must be determined experimentally to calculate the thrust from the measured force. A MicroEpsilon ILD1420 is mounted in front of the impingement plate to measure the displacement of the center of the impingement plate. The displacement response of the plate should then be measured for a disturbance (tap or blow on the back of the impingement plate. The natural frequency of the impingement plate is calculated from the period of the damped vibration response and the spring

constant of the impingement plate is calculated from the natural frequency as shown in the equations below.

$$\omega_n = \frac{2\pi}{t}$$

$$k_p = \omega_n{}^2 m$$

where t is the period of the response, ω_n is the natural frequency, and m is the mass of the impingement plate.

Thrust Stand Schematic and Operation

The figure below gives an electrical schematic of the thrust stand and the cold-gas capillary thruster used for benchmarking. A FemtoTools FT-S100 force probe is mounted on a Newport AG-LS25V6 motion stage behind the impingement plate and moved into a position where it is barely making contact at the center of the back ridge of the plate frame such that the thrust causes an increase in force measured by the probe. The FT-S100 has a range of up to 100 μN and a resolution of 5 nN. However, below ~10 μN the signal-to-noise ratio becomes much too small for measurements to be made from the raw signal. To increase the resolution of the thrust stand, the force probe is connected to an SRS SR830 Lock-In Amplifier which can detect signals which occur at the reference frequency of the amplifier at noise-to-signal ratios up to 1000-1. The lock-in amplifier outputs a 5 V square wave signal which is used to pulse the thruster at the reference frequency.

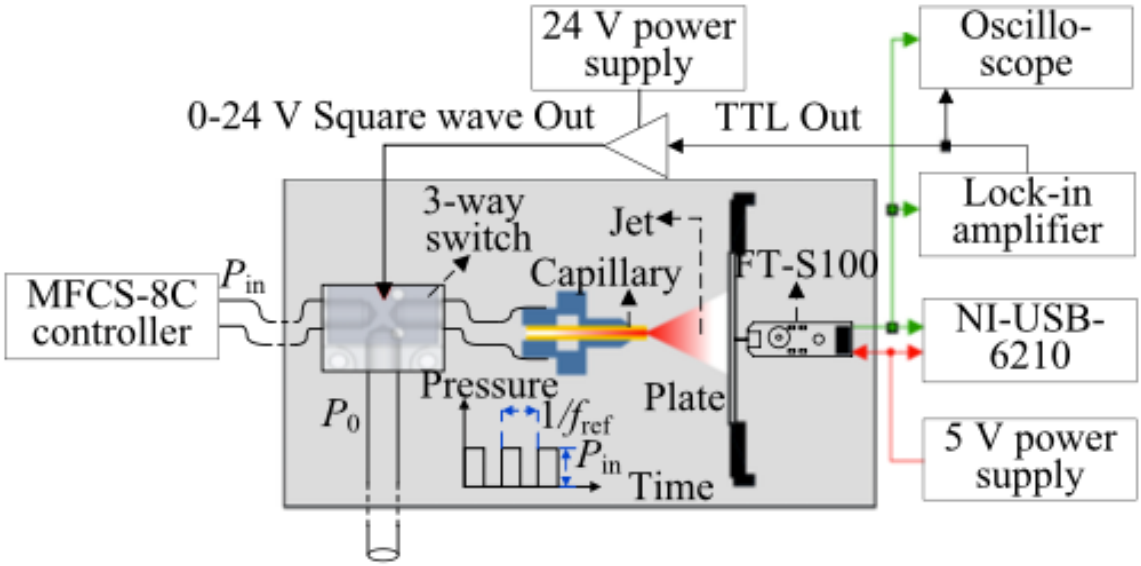

A 150 μm inner diameter capillary tube is connected to an SMC V114-SG 3-port solenoid valve with one input connected to a Proportion Air QPV series pressure regulator and the other input open to atmospheric pressure. The solenoid valve is triggered between atmosphere and the pressure regulator at the reference frequency to create thrust across the capillary at 50% duty cycle at the reference frequency. The figure on the left shows raw data collected from the force probe (blue) with a moving average (red) superimposed to shows the square wave shape of the thrust pulse. This data is fed into the Lock-In amplifier set to a 3 second time constant and 24 dB/octave phase sensitive detector (PSD) which locks into the signal at the 4 Hz reference frequency. The figure on the right shows the lock-in amplifier output over time. The signal rises from 10-40 seconds as it locks into the amplitude of the square wave force probe signal, the signal reaches steady-state from 40-80 seconds, and then the thruster is turned off at 80 seconds and the signal falls from 80-100 seconds.

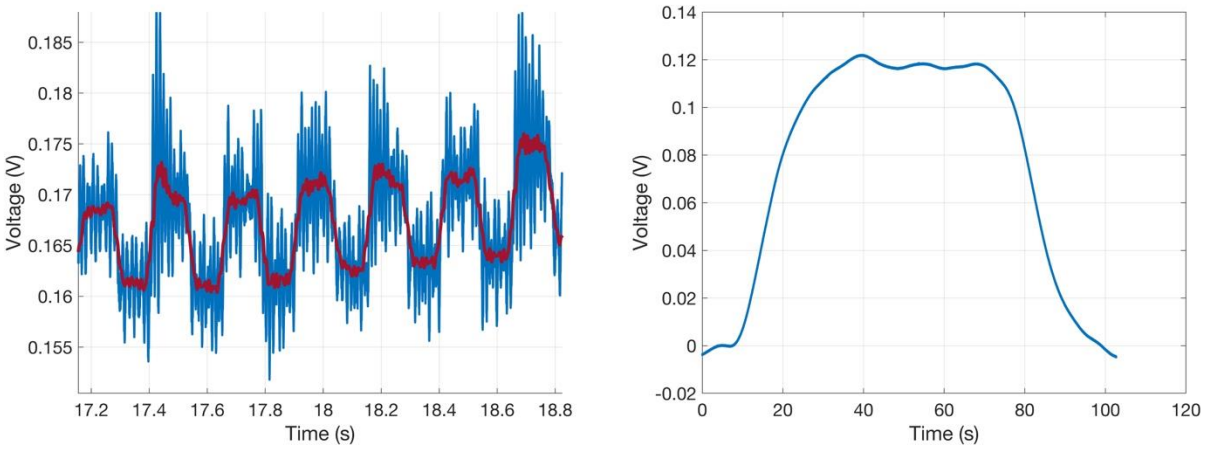

The lock-in amplifier signal is averaged over the steady-state period and used to calculate the impingement force using the equation below.

$$F = \frac{\pi}{\sqrt{2}}\left(1 + \frac{k_p}{k_f}\right) S_f R_{out}$$

where S_f is the sensitivity of the force probe in N/V and R_{out} is the average output of the lock-in amplifier.

Data Collected

The figures below show the Thrust vs. Pressure data collected at UIUC and by Chakraborty et. al.. The data agree very well down to 100 nN where the data collected at UIUC becomes subject to a noise floor. Further investigation revealed that this was due to the click of the solenoid valve causing vibration of the force probe at the reference frequency. Proper vibration isolation of the thrust stand from the surrounding equipment and environment should resolve this issue.

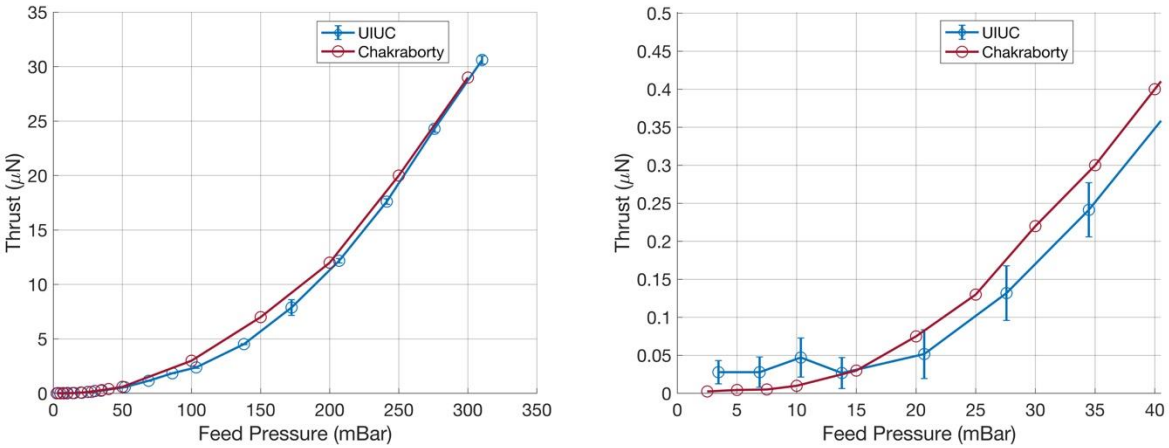

After the collection of the data presented above, the result could not be repeated on the following days of testing. Further data collection resulted in thrust measurements that were 4-5x higher than expected as illustrated in the figure below.

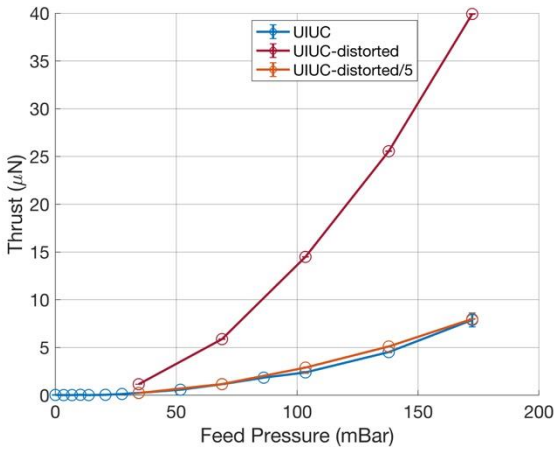

The source of this distortion has not been identified, but the measurements from the lock-in amplifier match the measurements from the raw force probe data peak-to-peak value and the force probe was confirmed to be measuring the correct forces by turning the thrust stand such that the impingement plate is facing up and placing small weights on top of it. It is possible that an issue with the benchmarking cold-gas capillary thruster itself was the issue and the thrust stand was operating correctly. Further investigation and experimentation are necessary to complete the construction of the thrust stand at UIUC.

APPENDIX E

XPS SPECTRA

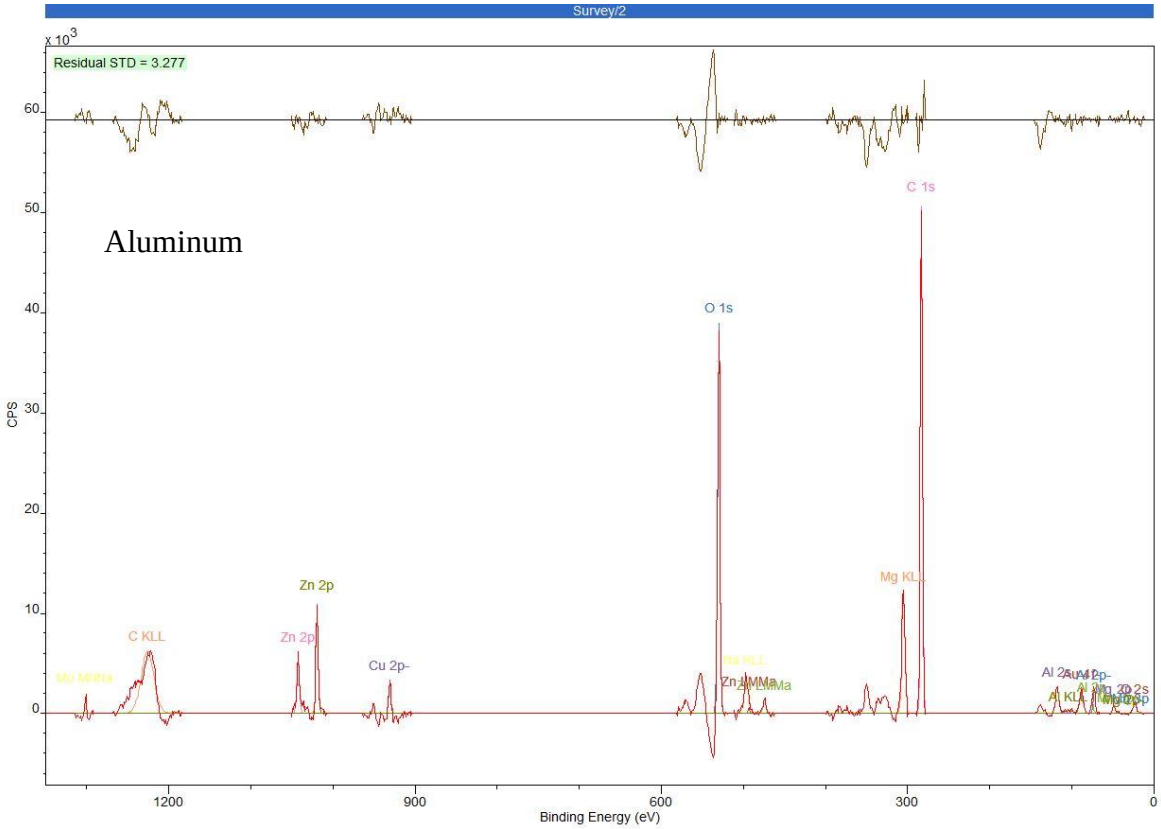

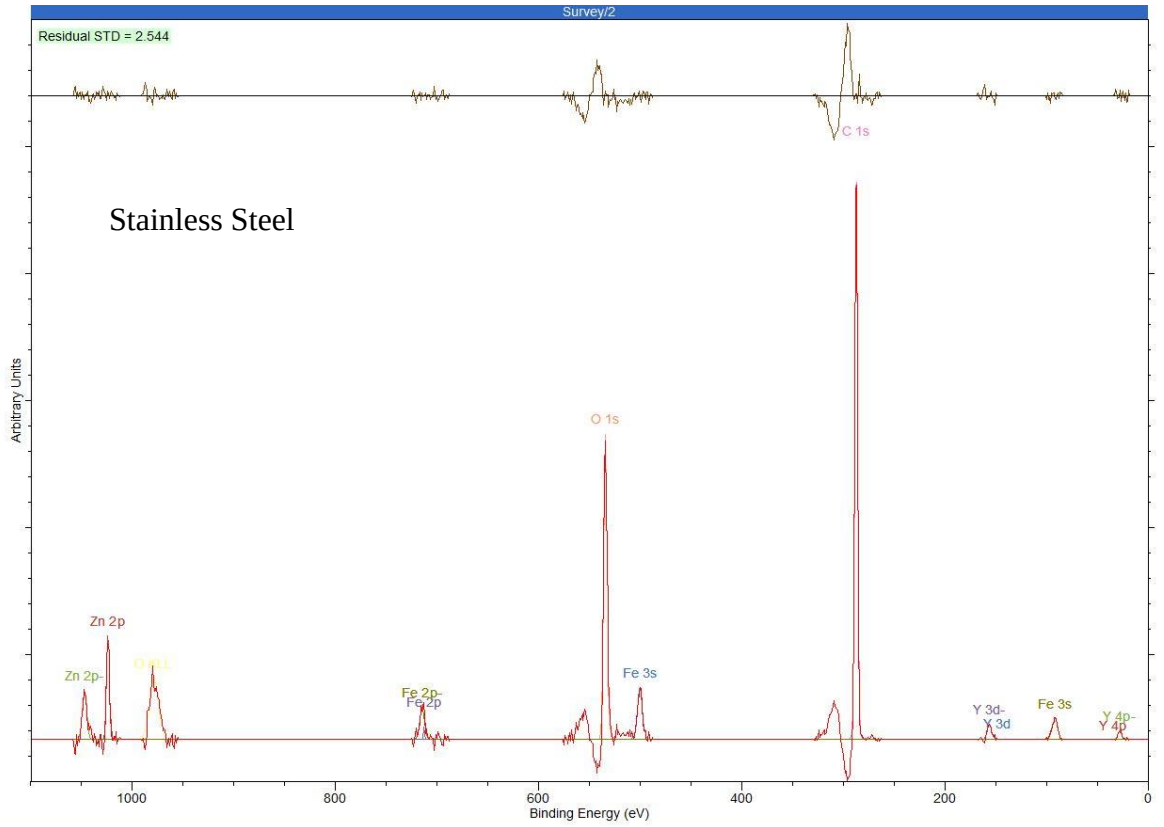
Survey/2
Residual STD = 2.544
Stainless Steel
C 1s
O 1s
Zn 2p
Zn 2p-
O KLL
Fe 2p-
Fe 2p
Fe 3s
Y 3d-
Y 3d
Fe 3s
Y 4p-
Y 4p
Arbitrary Units
1000
800
600
400
200
0
Binding Energy (eV)

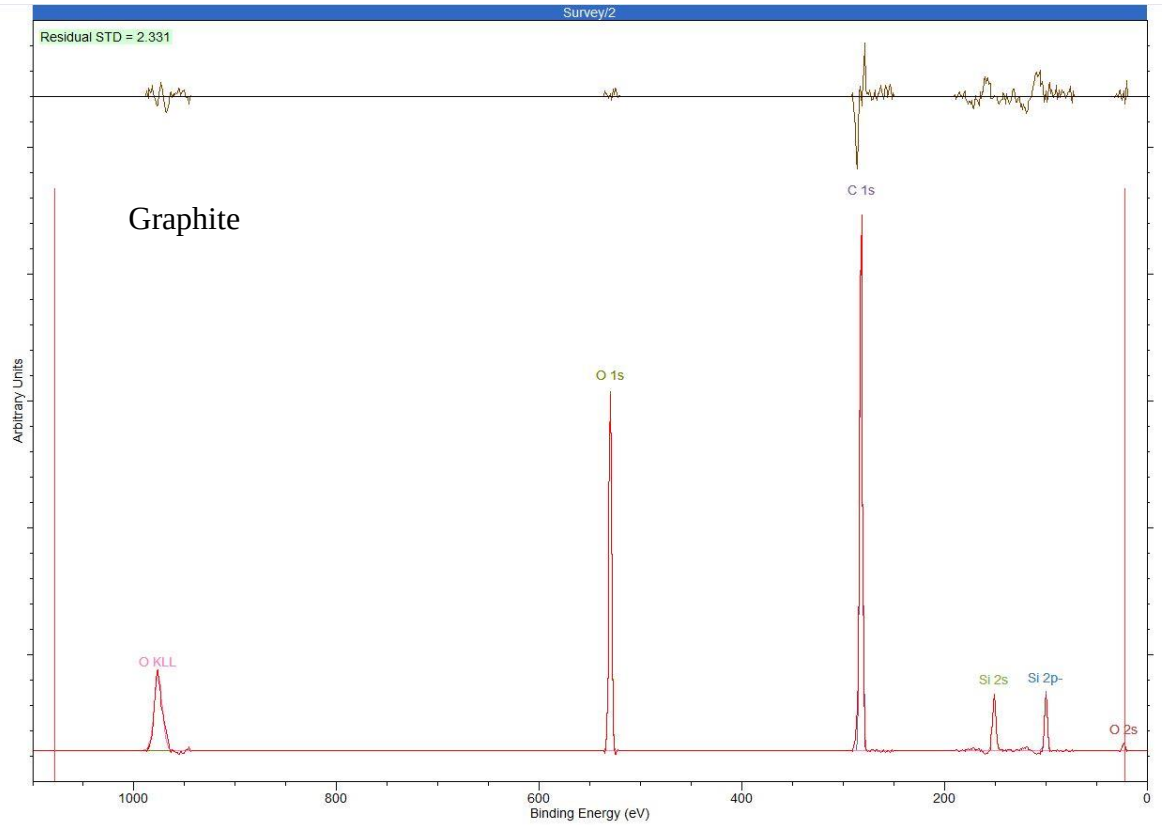
Survey/2
Residual STD = 2.331
Graphite
C 1s
O 1s
O KLL
Si 2s
Si 2p-
O 2s
Arbitrary Units
1000
800
600
400
200
0
Binding Energy (eV)

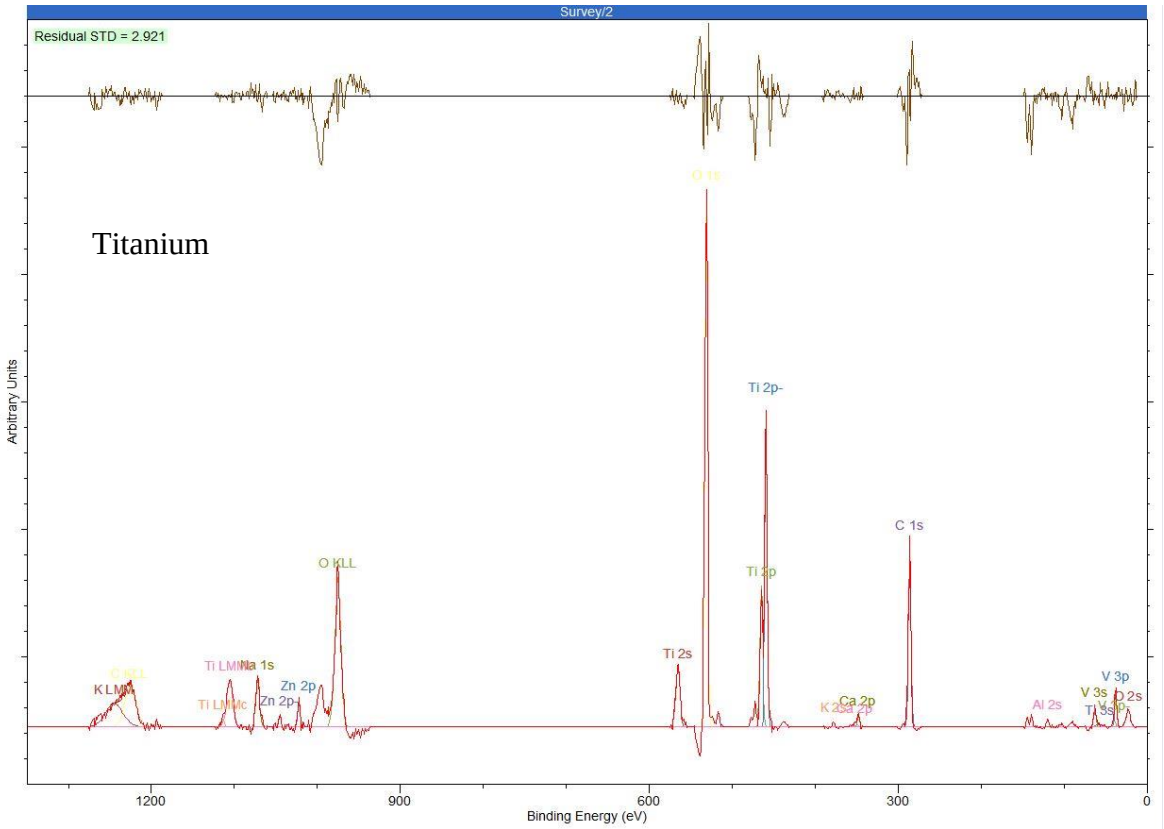
Survey/2
Residual STD = 2.921
Titanium
Arbitrary Units
O 1s
Ti 2p-
C 1s
O KLL
Ti 2p
Ti 2s
Na 1s
Zn 2p
Ca 2p
Al 2s
V 3p
V 3s
O 2s
1200
900
600
300
0
Binding Energy (eV)

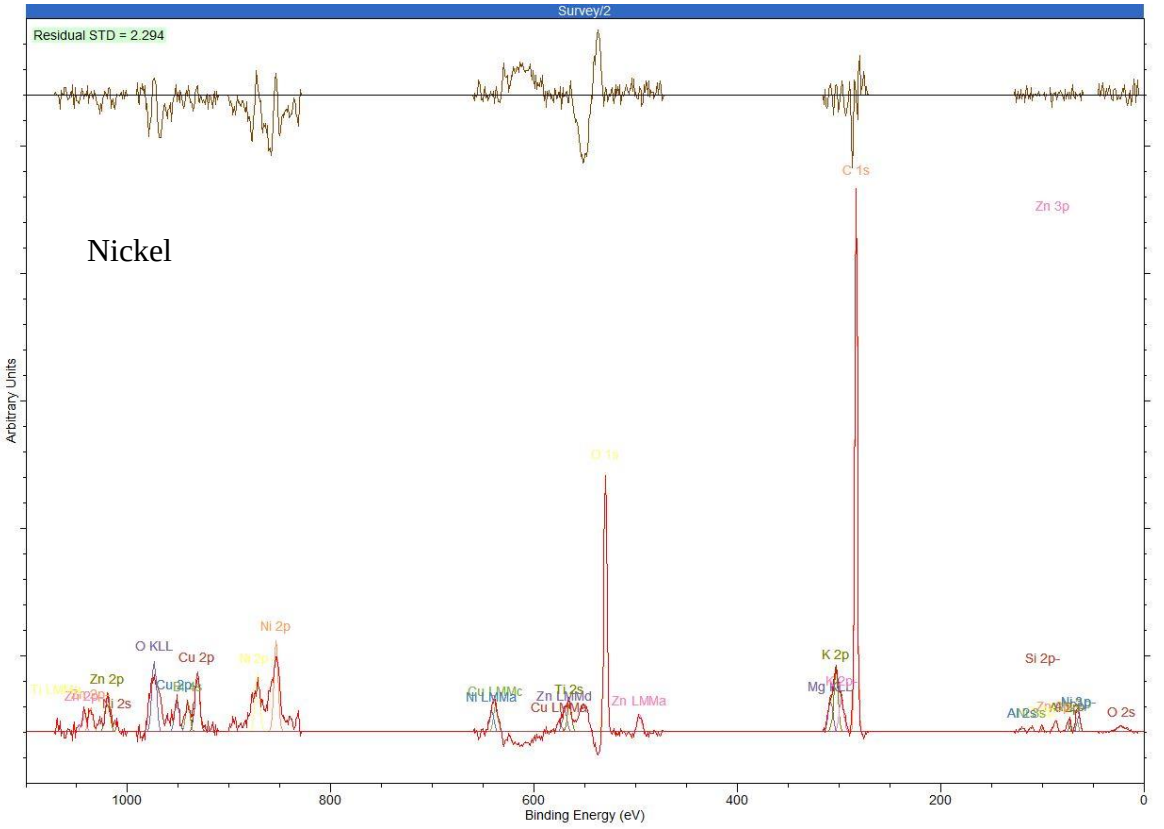
Survey/2
Residual STD = 2.294
Nickel
Arbitrary Units
C 1s
Zn 3p
O 1s
Ni 2p
O KLL
Cu 2p
Zn 2p
Ti 2s
Zn LMMa
K 2p
Si 2p-
O 2s
1000
800
600
400
200
0
Binding Energy (eV)

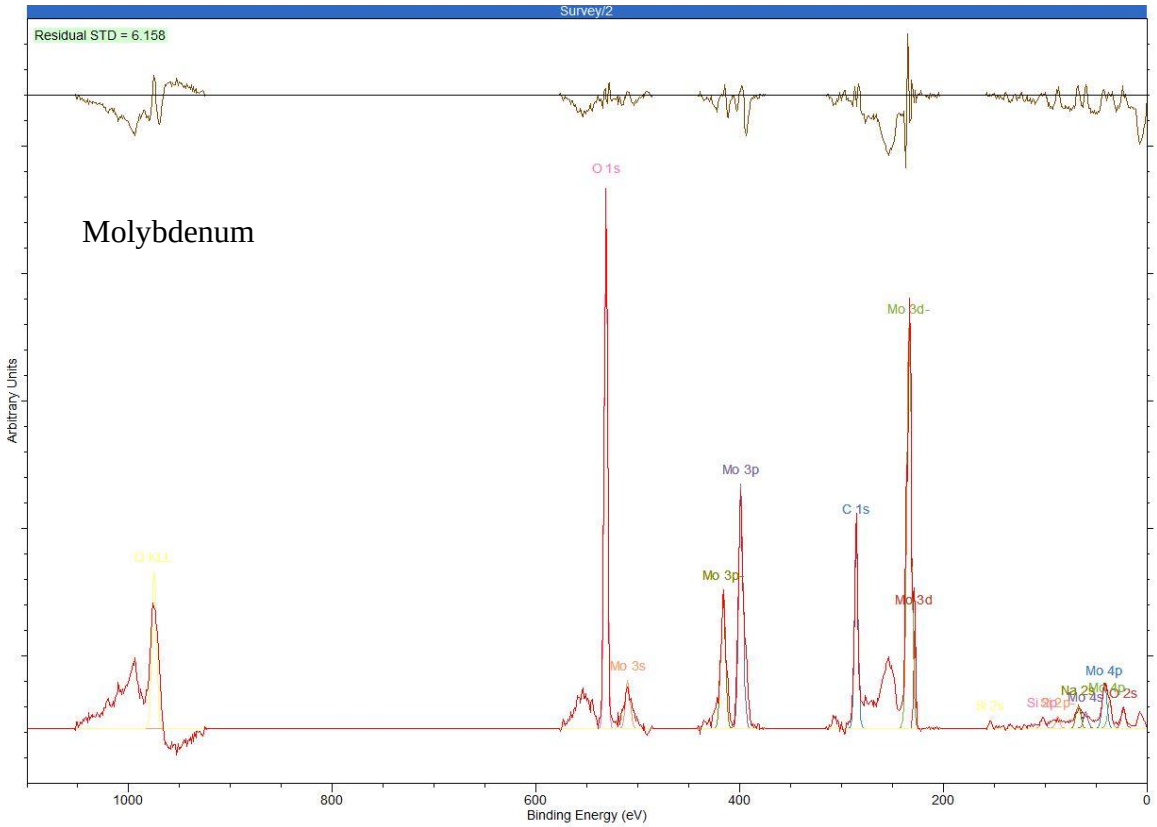
Survey/2
Residual STD = 6.158
Molybdenum
O 1s
Mo 3d-
Mo 3p
C 1s
O KLL
Mo 3p-
Mo 3d
Mo 3s
Mo 4p
Arbitrary Units
1000
800
600
400
200
0
Binding Energy (eV)

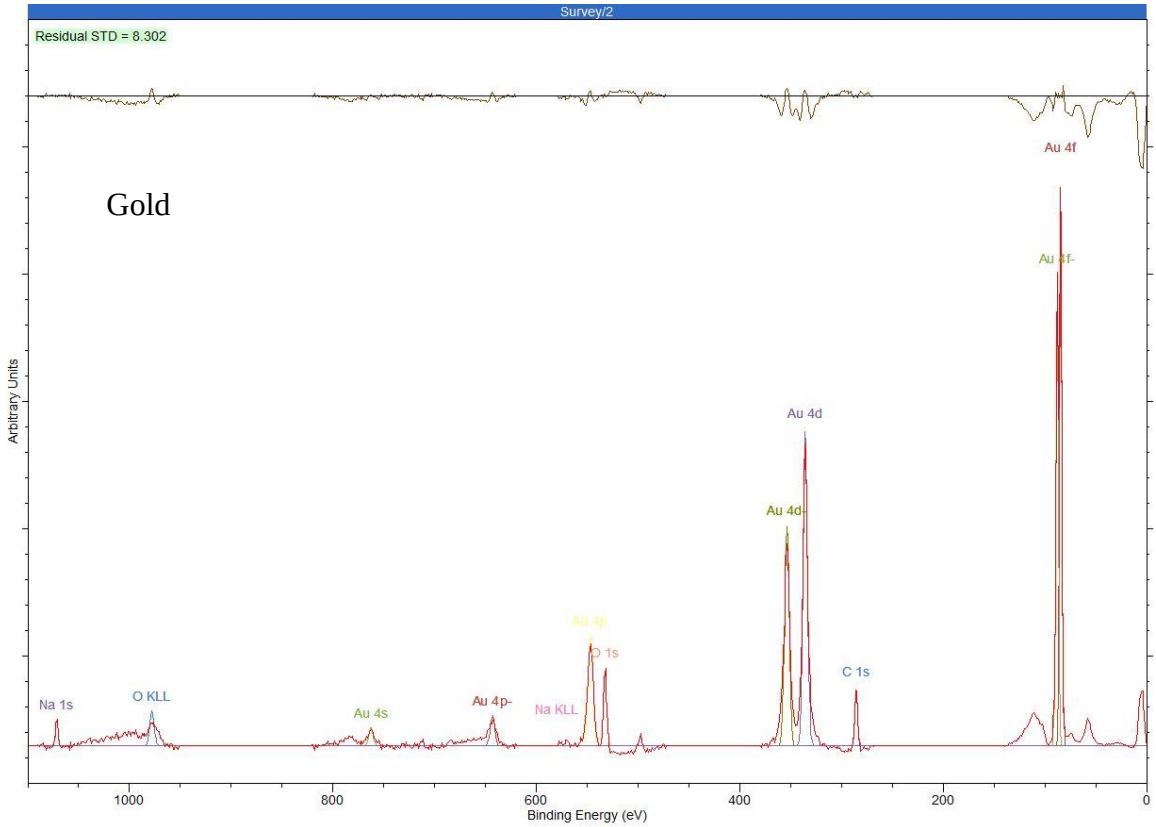
Survey/2
Residual STD = 8.302
Gold
Au 4f
Au 4d
Au 4d-
Au 4p
O 1s
C 1s
Na 1s
O KLL
Au 4s
Au 4p-
Na KLL
Arbitrary Units
1000
800
600
400
200
0
Binding Energy (eV)